Fluctuation Spectrum and Transport from Ion Temperature Gradient Driven Modes in Sheared Magnetic Fields

Satoshi Hamaguchi and *Wendell Horton*
Institute for Fusion Studies
The University of Texas at Austin
Austin, Texas 78712

August 1989

Fluctuation Spectrum and Transport from Ion Temperature Gradient Driven Modes in Sheared Magnetic Fields

Satoshi Hamaguchi and Wendell Horton
Institute for Fusion Studies
The University of Texas at Austin
Austin, Texas 78712

Abstract

The ion temperature gradient driven mode or η_i-mode turbulence is reinvestigated based on two component compressible fluid equations with the polarization drift velocity and adiabatic electrons. The scaling of the anomalous ion heat conductivity with magnetic shear $s = L_n/L_s$ and the excess of η_i over the critical value $\eta_{i,c}$ for marginal stability is found to vary as $\chi_i = g(\rho_s/L_n)(cT_i/eB)(\eta_i - \eta_{i,c})\exp(-\alpha s)$, where $g = \mathcal{O}(1)$ and $\alpha \simeq 5$.

I. Introduction

Recent experimental studies in tokamaks both with regard to the ion thermal confinement properties[1-3] and with respect to the fluctuation spectrum[4] indicate that the ion temperature gradient driven drift mode or η_i-mode[5,6] is probably a determining part of the thermal confinement properties in tokamaks. In view of these experimental developments we reconsider some of the theoretical differences[7-10] that are found in the earlier formulas for the η_i-mode turbulence and the associated anomalous ion heat conductivity χ_i. In particular we investigate the magnetic shear $s = L_n/L_s$ dependence of the anomalous heat conductivity $\chi_i(s)$. Here L_n and L_s denote the scaling lengths of the density gradient and the magnetic shear, respectively. The early 3D nonlinear study of Horton-Estes-Biskamp[7] reports that χ_i decreases weakly as $s^{-1/2}$ with increasing shear, whereas the subsequent theoretical works of Connor,[8] Lee and Diamond,[9] and Terry, et al.[10] indicate the opposite tendency with χ_i increasing linearly with the shear s. In the work of Connor,[8] such scaling of χ_i was derived using the dimensional analysis of a system further simplified from the original sheared slab model of the η_i-mode. In the work of Lee and Diamond[9] and the work of Terry et al.[10] the authors essentially attempt to explain the shear dependence of χ_i with the linear growth rate increasing linearly with the shear s under the assumption of small poloidal mode numbers ($k_y^2 \rho^2(\eta_i + 1) \ll 1$ with k_y being the ion poloidal wavenumber, ρ being the ion Larmor radius, $\eta_i = L_n/L_T$ and L_T being the scale length of the ion temperature gradient) and fixed radial eigenmode numbers ℓ. The dependence of χ_i on the ion temperature gradient η_i is also of basic importance. In these previous works the η_i-dependence of χ_i scales as $\chi_i \propto (\eta_i + 1)^\alpha$ with $1/2 \lesssim \alpha \leq 2$. Since the model equations of the η_i-mode on which all these previous results are based are the same,[11] the correct scaling of the ion anomalous heat transport χ_i due to the slab η_i-mode turbulence has not been established yet.

In order to settle this discrepancy, we reinvestigate the problem using more rigorous analyses and numerical simulations based on the same two component compressible fluid equations with adiabatic electrons. The parameter regime of interest is $s \ll 1$ and finite L_n, a typical parameter regime of high temperature tokamak plasmas. We solve the linear eigenvalue problem analytically with perturbation theory and numerically with the shooting code and the initial-value code. Based on the space-time scale obtained from the linear analysis, mixing length theory is applied to estimate the anomalous ion heat conductivity, which is then compared to the results of the amplitude expansion method and numerical simulations. In the amplitude expansion method, the set of nonlinear equations of the η_i-mode is solved rigorously near the marginally stable state, and the dependence of χ_i on the ion temperature gradient η_i is obtained. The nonlinear initial-value code is used to solve the 2D and 3D equations for the finite amplitude fluctuations. In the steady-state of turbulence the scaling of the anomalous ion heat conductivity $\chi_i(s, \eta_i)$ is obtained for a wide range of the parameter space. The simulations use a second order finite difference formula in the radial direction x and Fourier component representations in the perpendicular y- and z-directions. This numerical method contrasts with the finite difference formulas in the three-space directions with up-wind derivatives in the $\mathbf{E} \times \mathbf{B} \cdot \nabla$ nonlinearity used by Horton, Estes and Biskamp.[7]

An important feature of the stability analysis is that the linear mode is most strongly excited when $k_y \rho_s \simeq (1+\eta_i)^{-1/2}$ and $(2\ell+1)s \simeq$ const. It then follows that the growth rate of the fastest growing mode γ_m is a weakly decreasing function of the shear while localization of the mode around the mode rational surface becomes stronger with increasing shear s. Suppose such strongly excited linear modes are responsible for the nonlinearly saturated turbulent state, the associated anomalous ion heat transport is expected to decrease with increasing shear, unlike the χ_i-scalings reported in Refs. 8-10. While numerical simulations show that the peak of energy spectrum is downshifted from the wavenumber giving the fastest

3

growing linear mode, the mixing length estimate based on the most unstable linear mode provides the general tendency of the χ_i-scaling that agrees reasonably well with the numerical results. Physically, this is expected since the fastest growing linear mode is the energy input to the turbulence. Based on a more rigorous nonlinear analysis and parameterization of the numerical results, we find that the anomalous ion heat conductivity is given by

$$\chi_i = g \frac{\rho_s}{L_n} \left(\frac{cT_i}{eL_n} \right) (\eta_i - \eta_{i,c}) \exp(-\alpha s) \tag{1}$$

with $g = \mathcal{O}(1)$, $\alpha \simeq 5$ and $\eta_{i,c}$ denoting the critical η_i-value. In deriving the shear dependence $\chi_i(s)$ in Eq. (1), we consider both power law s^β and exponential fits. With the alternative power law parameterization of $\chi_i(s)$ we obtain $\beta = -2$ for $s \gtrsim 0.5$, as in resistive g-mode turbulence, and $\beta = -1/2$ for $s \simeq 0.1$. As shown in Sec. V, the exponential dependence fits well the entire range of shear. It is found that the scaling obtained by Horton, Estes and Biskamp[7] agrees reasonably well with the scaling above in the limited range of the shear parameter $0.05 \lesssim s \lesssim 0.1$ while it underestimates the strength of the shear dependence for larger shear. On the other hand, the scalings of Connor,[8] Lee and Diamond[9] and Terry et al.[10] ($\beta = 1$) give the wrong qualitative dependence on the shear with χ_i increasing with increasing shear.

For smaller shear, the locally unfavorable toroidal curvature $\varepsilon_n = L_n/R$ effects are dominant[12-16] and the sheared slab model of the η_i-mode becomes no longer applicable. The anomalous ion heat conductivity χ_i calculated by Horton, Choi and Tang[12] from the toroidal η_i-mode, however, also shows that χ_i is a decreasing function of shear, scaling as $\chi_i \propto 1/s$. In the work of Hong and Horton,[17] the limit $s \to 0$ of the toroidal η_i-mode is reexamined. For sufficiently small shear, the radial profile of the electron diamagnetic frequency $\omega_*(r)$ and the ion temperature gradient $\eta_i(r)$ must be taken into account over the mode width Δr.

The present work is organized as follows. In Sec. II we give the non-dimensional field

variables and the dynamical equations along with their conservation properties. In Sec. III the linear analysis is presented, in particular, assessing the shear stabilization effect due to the parallel compressibility and the parallel diffusion. In Sec. III we also present the mixing length estimate, deriving as a reference formula the anomalous ion heat conductivity $\chi_i(s, \eta_i)$ of the η_i-mode turbulence. In Sec. IV, the amplitude expansion method is used to solve the nonlinear equations and the η_i-dependence of χ_i is obtained. The results of the 2D and 3D numerical simulations are shown in Sec. V and the scaling of χ_i is derived therein. The conclusions and brief critiques to the previous results are given in Sec. VI.

II.   Dynamical Equations

In this section we present the dynamical equations of the ion temperature gradient driven mode and review their basic properties. The fluid model of the electrostatic ion temperature gradient driven mode in a sheared slab is derived[7] from the two-component fluid equations (Braginskii equations)[18] with the finite ion Larmor radius stress tensor and the ion heat balance equation. Assuming charge neutrality, constant electron temperature and zero electron inertia, the parallel component of the electron momentum balance equations is used to derive a Boltzman distribution of electrons

$$n = n_i = n_e = n_0(x) \left(1 + \frac{e\Phi}{T_e}\right) \, , \tag{2}$$

where n_i and n_e are the ion and electron densities, respectively, $n_0(x)$ is the unperturbed density, $\Phi = \Phi(x, y, z, t)$ is the electric potential, $e(e > 0)$ is the magnitude of the electron charge and T_e is the (constant) electron temperature. In Eq. (2) we assumed that $|e\Phi/T_e| \ll 1$. The coordinate system (x, y, z) is the usual orthogonal coordinate system represented by three unit vectors $\hat{x}, \hat{y}$ and $\hat{z}$. Here $\hat{x}$ represents the radial direction of a plasma cylinder, $\hat{z}$ represents the direction of the magnetic field $\mathbf{B}$ at a rational surface, the position of which is indicated by $x = x_0$. To the lowest order, the ion fluid velocity $\mathbf{v}$ may be written as the

sum of the $\mathbf{E} \times \mathbf{B}$ drift velocity $\mathbf{v}_E$ and the ion diamagnetic drift velocity $\mathbf{v}_D$, where

$$\mathbf{v}_E = c \frac{\mathbf{E} \times \mathbf{B}}{B^2}$$

and

$$\mathbf{v}_D = c \frac{\hat{\mathbf{z}} \times \nabla p_i}{enB} .$$

Here $\mathbf{E} = -\nabla \Phi$ is the electric field, c is the light velocity, $B = |\mathbf{B}|$ is the magnitude of the magnetic field at $x = x_0$ and p_i is the ion pressure. To the next order of $\mathbf{v}$, we have the polarization drift velocity

$$\mathbf{v}_p = \frac{-c^2 m_i}{eB^2} \left(\frac{\partial}{\partial t} + (\mathbf{v}_E + \mathbf{v}_D) \cdot \nabla \right) \nabla_\perp \Phi , \tag{3}$$

where m_i is the ion mass and $\nabla_\perp$ is the gradient perpendicular to the direction of the magnetic field $\mathbf{B}$. Denoting the parallel velocity by $v_\parallel$, we write

$$n = n_0(x) + \tilde{n}_i = n_0 + n_0 e\Phi/T_e$$

$$p_i = p_{i0}(x) + \tilde{p}_i$$

$$\Phi = \tilde{\Phi} \qquad \text{and} \qquad v_\parallel = \tilde{v}_\parallel ,$$

where the subscript 0 denotes the unperturbed quantities which are assumed to be functions of only x, and the tilde denotes the fluctuating quantities. Here we assume that the unperturbed parts of the velocity field $\mathbf{v}$ and the potential Φ are zero. In order to write down the dynamical equations in a nondimensional form, we define the following characteristic velocity and space scales,

$$c_s = \left(\frac{T_e}{m_i} \right)^{1/2} \quad , \quad \rho_s = \frac{c_s}{\omega_{ci}} = \frac{c(m_i T_e)^{1/2}}{eB} ,$$

$$L_n = -\left(\frac{d}{dx} \ell n \, n_0 \right)^{-1} \quad , \quad L_T = -\left(\frac{d}{dx} \ell n \, T_{i0} \right)^{-1} ,$$

6

and the nondimensional parameters

$$\eta_i = \frac{L_n}{L_T} \quad , \quad K = \frac{T_i}{T_e}(1 + \eta_i) \quad , \quad \Gamma = \frac{\gamma T_i}{T_e} \, . \tag{4}$$

Here γ denotes the ratio of the specific heats, ω_{ci} is the ion cyclotron frequency and all the unperturbed quantities are again evaluated at $x = x_0$. In the present work, we assume that $\mathcal{O}(\eta_i) = 1$ so that $L_n(\simeq L_T)$ is the typical macroscopic length of the system. It is known[19,20] that, in the case of the flat density profile ($L_n \gg L_T$), the η_i-mode has different properties. The appropriate nondimensional space-time variables are

$$\tilde{x} = \frac{x - x_0}{\rho_s} \quad , \quad \tilde{y} = \frac{y}{\rho_s} \quad , \quad \tilde{z} = \frac{z}{L_n} \quad , \quad \tau = \frac{tc_s}{L_n} \, .$$

Assuming that the fluctuation level is small in the sense that the ratios $\tilde{n}/n_0$, $\tilde{v}_\parallel/c_s$, $\tilde{p}_i/p_{i0}$ and $e\tilde{\Phi}/T_e$ are of order of ρ_s/L_n, and the fluctuating quantities vary more rapidly in space than the corresponding unperturbed quantities, the nonlinear evolution equations of the fluctuations are given by

$$(1 - \nabla_\perp^2)\frac{\partial \phi}{\partial \tau} = -\left(1 + K \nabla_\perp^2\right)\frac{\partial \phi}{\partial \tilde{y}} - \nabla_\parallel v + \{\phi, \nabla_\perp^2 \phi\} - \mu_\perp \nabla_\perp^4 \phi \tag{5}$$

$$\frac{\partial v}{\partial \tau} = -\nabla_\parallel(\phi + p) - \{\phi, v\} + \mu_\perp \nabla_\perp^2 v + \mu_\parallel \nabla_\parallel^2 v \tag{6}$$

$$\frac{\partial p}{\partial \tau} = -K \frac{\partial \phi}{\partial \tilde{y}} - \Gamma \nabla_\parallel v - \{\phi, p\} + \chi_\perp \nabla_\perp^2 p + \chi_\parallel \nabla_\parallel^2 p \, , \tag{7}$$

where only the $\mathbf{E} \times \mathbf{B}$ convective nonlinear terms are retained as nonlinearity for simplicity. It is shown in Ref. 7 that the other nonlinearities arising from $v_\parallel \nabla_\parallel \mathbf{v}$ and $v_\parallel \nabla_\parallel p$ are negligible if $\rho_s/a \ll 1$. Here the dependent variables are defined by

$$\phi = \frac{e\tilde{\Phi}}{T_e} \cdot \frac{L_n}{\rho_s}$$

$$v = \frac{\tilde{v}_\parallel}{c_s} \cdot \frac{L_n}{\rho_s}$$

$$p = \frac{\tilde{p}_i}{p_{i0}} \cdot \frac{L_n}{\rho_s} \, ,$$

7

all of which are of order of unity, the Poisson bracket $\{f, g\}$ and the perpendicular gradient $\nabla_\perp$ are defined by

$$\{f, g\} = \hat{\mathbf{z}} \cdot \nabla_\perp f \times \nabla_\perp g = \frac{\partial f}{\partial \widetilde{x}} \frac{\partial g}{\partial \widetilde{y}} - \frac{\partial f}{\partial \widetilde{y}} \frac{\partial g}{\partial \widetilde{x}}$$

$$\nabla_\perp = \frac{\partial}{\partial \widetilde{x}} \hat{\mathbf{x}} + \frac{\partial}{\partial \widetilde{y}} \hat{\mathbf{y}} . \tag{8}$$

In deriving Eqs. (5)–(7), the magnetic field is assumed to take the form

$$\mathbf{B} = B \left(\hat{\mathbf{z}} + \frac{x - x_0}{L_s} \mathbf{y} \right) ,$$

where L_s is the shear length. With the definition of the shear parameter $s = L_n / L_s$, the parallel derivative $\nabla_\parallel$ in Eqs. (5)–(7) may be written as

$$\nabla_\parallel = \frac{\partial}{\partial \widetilde{z}} + s\widetilde{x} \frac{\partial}{\partial \widetilde{y}}. \tag{9}$$

The constants $\mu_{\perp,\parallel}$ and $\chi_{\perp,\parallel}$ in Eqs. (5)–(7) are appropriately chosen dissipation rates. For collisional plasma the values of μ and χ may be taken from Coulomb transport theory.[11] For the high temperature tokamak plasmas of interest the appropriate choice of $\mu_\parallel$ and $\chi_\parallel$ is to model the collisionless ion Landau effect.

The domain on which Eqs. (5)–(7) are solved is given by the cubic box $|\widetilde{x}| \le L_x$, $0 \le \widetilde{y} \le L_y$ and $0 \le \widetilde{z} \le L_z$, L_y and L_z being constants of order unity. The size of the box in the x direction L_x is taken to be large enough, so that when there is magnetic shear ($s \ne 0$), single helicity modes localized at $\widetilde{x} = 0$ decay sufficiently as $|\widetilde{x}| \to L_x$. In the case of zero shear $2L_x$ represents the width of the constant background ion pressure gradient and/or the constant background density gradient. For the boundary conditions of Eqs. (5)–(7), all the dependent variables are assumed to vanish at $|\widetilde{x}| = L_x$ and to be periodic in the $\widetilde{y}$ and $\widetilde{z}$ directions.

We define the space average $\langle \quad \rangle$ by

$$\langle \quad \rangle = \frac{1}{2L_x L_y L_z} \int_{-L_x}^{L_x} d\widetilde{x} \int_0^{L_y} d\widetilde{y} \int_0^{L_z} d\widetilde{z} , \tag{10}$$

8

and we introduce the averaged fluctuation energy densities

$$E_\phi = \frac{1}{2} \left\langle \phi^2 + |\nabla_\perp \phi|^2 \right\rangle$$

$$E_v = \frac{1}{2} \left\langle v^2 \right\rangle \qquad \text{and} \qquad E_p = \frac{1}{2} \left\langle p^2 \right\rangle .$$

The energy transfer rates between the three energy densities are given by the compressional work W_{comp} done by $\nabla_\| v$

$$W_{\text{comp}} = \left\langle p \, \nabla_\| v \right\rangle ,$$

and the $j_\| E_\|$ work done on the parallel ion current $j_\| \equiv e v_\|$

$$W_{jE} = - \left\langle v \nabla_\| \phi \right\rangle .$$

It follows from Eqs. (5)–(7) that the energy transfer equations are given by

$$\frac{dE_\phi}{dt} = -W_{jE} - \mu_\perp \left\langle |\nabla_\perp^2 \phi|^2 \right\rangle$$

$$\frac{dE_v}{dt} = W_{jE} + W_{\text{comp}} - \mu_\perp \left\langle |\nabla_\perp \phi|^2 \right\rangle - \mu_\| \left\langle (\nabla_\| v)^2 \right\rangle$$

and

$$\frac{dE_p}{dt} = KQ - \Gamma W_{\text{comp}} - \chi_\perp \left\langle |\nabla_\perp p|^2 \right\rangle - \chi_\| \left\langle (\nabla_\| p)^2 \right\rangle ,$$

where

$$Q = \left\langle p \frac{\partial \phi}{\partial y} \right\rangle = - \left(\frac{\rho_s}{L_n} \frac{cT_e}{eB} \frac{p_{i0}}{L_n} \right)^{-1} \left\langle \tilde{p}_i \, \tilde{v}_{Er} \right\rangle \tag{11}$$

is the anomalous ion heat flux across the magnetic flux surface and $\tilde{v}_{Er} = \mathbf{v}_E \cdot \nabla r$. These anomalous transfers W_{jE} and W_{comp} take energy out of the thermal ions and produce a growth of E_p, E_v, and E_ϕ. The source of the turbulence arises from the unperturbed ion pressure gradient

$$K = -\frac{dp_{i0}}{dx} \frac{L_n}{n_0 T_e} = \frac{T_i}{T_e} (1 + \eta_i)$$

9

which drives the total fluctuation energy density

$$E_T = E_\phi + E_v + \frac{1}{\Gamma} E_p \qquad (12)$$

with

$$\frac{dE_T}{dt} = \frac{KQ}{\Gamma} - \sum_\alpha P_\alpha \qquad (13)$$

where P_α are the dissipation rates given by

$$P_1 = \mu_\perp \left\langle (\nabla_\perp^2 \phi)^2 \right\rangle \;\; , \;\; P_2 = \mu_\perp \left\langle |\nabla_\perp v|^2 \right\rangle$$

$$P_3 = \mu_\parallel \left\langle |\nabla_\perp v|^2 \right\rangle \;\; , \;\; P_4 = \chi_\perp \left\langle |\nabla_\perp p|^2 \right\rangle$$

$$P_5 = \chi_\parallel \left\langle (\nabla_\parallel p)^2 \right\rangle \; .$$

In the turbulent steady state the free-energy production KQ/Γ is balanced by the energy absorption given by $\sum_\alpha P_\alpha$ in Eq. (13).

III.   Linear Stability Theory and Mixing Length Theory

Having presented the dynamical equations of the η_i-mode in the preceding section, we examine the linear properties of the system, especially focusing on the shear stabilization effect associated with plasma compressibility and parallel diffusion. We also attempt to clarify the physical meaning of the η_i-mode using the local approximation of the linearized system, which will serve as the basis of physical interpretation of our conclusions discussed in Sec. VI.

10

A. Local Stability Theory

In the local approximation, in which $\partial/\partial \tilde{x}$ and $\nabla_\parallel$ are replaced by constants $i\tilde{k}_x$ and $i\tilde{k}_\parallel$, respectively, the linear dynamics of Eqs. (5)–(7) is given by the dispersion relation

$$(1 + \tilde{k}_\perp^2)\,\tilde{\omega}^2 - \tilde{k}_y\,\tilde{\omega}(1 - K\,\tilde{k}_\perp^2) - \frac{\tilde{k}_\parallel^2\left(1 - \frac{K\tilde{k}_y}{\omega}\right)}{1 - \frac{\Gamma\tilde{k}_\parallel^2}{\tilde{\omega}^2}} = 0 \ . \tag{14}$$

Here $\tilde{y}$, $\tilde{z}$ and τ dependence of the independent variables are assumed to be $\exp\, i(\tilde{k}_y\,\tilde{y} + \tilde{k}_z\,\tilde{z} + \tilde{\omega}\,\tau)$ and $\tilde{k}_\perp^2 = \tilde{k}_x^2 + \tilde{k}_y^2$. All the diffusion coefficients in Eqs. (5)–(7) are ignored in Eq. (14) for simplicity in the weakly dissipative, long wave length region. In the local approximation, the constant $\tilde{k}_\parallel$ models $\nabla_\parallel$ with the relation $\tilde{k}_\parallel = s\Delta_x\,\tilde{k}_y + \tilde{k}_z$, where Δ_x denotes a typical mode width in the x-direction. When the shear s is small, the parallel derivative $\nabla_\parallel$ is approximately given by the constant $\tilde{k}_z$ and the dispersion relation of the linearized system of Eqs. (5)–(7) is also approximately given by Eq. (14). In this case, the parallel dynamics is dominated by the effect of the periodicity in the $\tilde{z}$-direction rather than the $\tilde{y}$-direction. In the case of zero-shear, Eq. (14) becomes the exact dispersion relation of the linearized system of Eqs. (5)–(7) with the relation $\tilde{k}_\parallel = \tilde{k}_z$.

In the dimensional form, Eq. (14) may be written as

$$(1 + k_\perp^2\,\rho_s^2)\,\omega^2 - \omega\omega_e^*(1 - K\,k_\perp^2\,\rho_s^2) - \frac{k_\parallel^2\,c_s^2\left(1 - \frac{\omega_{pi}^*}{\omega}\right)}{1 - \frac{\Gamma\,k_\parallel^2\,c_s^2}{\omega^2}} = 0 \ , \tag{15}$$

where

$$\omega_e^* = \frac{c\,T_e}{eB}\,\frac{k_y}{L_n} \ ,$$

$$\omega_{pi}^* = -\frac{c\,T_i}{eB}\,\frac{k_y}{L_n}\,(1 + \eta_i) = -\omega_e^*\,K \ ,$$

$$k_\perp = \tilde{k}_\perp/\rho_s \ , \quad k_\parallel = \tilde{k}_\parallel/L_n \ , \quad \omega = c_s\,\tilde{\omega}/L_n \ .$$

Balancing the first term and the second term in Eq. (15) gives the dispersion of the drift wave, the frequency of which is downshifted from ω_e^* to

$$\omega_{\mathrm{k}}^{\mathrm{loc}} = \omega_e^*(1 - K\,k_\perp^2\,\rho_s^2)/(1 + k_\perp^2\,\rho_s^2) \tag{16}$$

for $|\omega_{\mathrm{k}}^{\mathrm{loc}}| \gg \Gamma^{1/2}\,k_\|\,c_s$. The downshift of the local frequency in Eq. (16) is due to the perpendicular compressibility in the continuity equation. When the ion pressure gradient effect $K\,k_\perp^2\,\rho_s^2$ is small, the wave traveling perpendicular to the field line propagates in the electron diamagnetic direction. The third term of Eq. (15) represents the ion acoustic wave coupled with the thermal mode arising from ω_{pi}^*. The modified sound velocity c_{sm} is given by

$$c_{sm} = c_s\left(1 - \omega_{pi}^*/\omega\right)^{1/2}\ ,$$

where the finite Γ effect or the parallel compressibility in Eq. (15) is ignored. Since the local modes (16) are low frequency mode ($|\omega| \ll |\omega_{pi}^*|$) for $|\omega_{pi}^*| \sim \omega_e^*$, the modified sound velocity becomes complex as ω becomes complex, which is the manifestation of the η_i-mode. We now estimate the growth rate from Eq. (15). For the mode with small perpendicular wavenumber $|k_\perp\,\rho_s| \ll K^{-1/2}$ and low frequency $|\omega| \ll \omega_e^* \sim |\omega_{pi}^*|$, the second and third terms become dominant, which give the complex eigenfrequencies

$$\omega \simeq i\,k_\|\,c_s\,\sqrt{K}\ . \tag{17}$$

However, by choosing the wavenumber $k_\perp$ in such a way that the first term becomes more dominant than the second term in Eq. (15), i.e., $k_\perp\,\rho_s = K^{-1/2}$, we obtain the complex frequencies

$$\omega \simeq (\omega_{pi}^*\,k_\|^2\,c_s^2)^{1/3}\qquad,\qquad \frac{-1 \pm i\,\sqrt{3}}{2}\,(\omega_{pi}^*\,k_\|^2\,c_s^2)^{1/3} \tag{18}$$

by balancing the first term with the third term in Eq. (15). Since modes with small parallel wavenumbers ($k_\|\,c_s \ll \omega_e^*$) are of interest, Eq. (18) gives larger growth rate than Eq. (17).

12

The parallel and perpendicular diffusion coefficients in Eqs. (5)–(7) significantly stabilize the modes with high wavenumbers. Taking into account the finite diffusion coefficients, we now solve numerically the more complicated dispersion relation obtained from Eqs. (5)–(7) under the local approximation. Figure 1 shows the contours of constant growth rate $\gamma = \text{Im}\,\omega$ as a function of k_y and $k_\parallel$ with finite diffusion coefficients. Since the maximum growth rate generally occurs for finite k_x, k_x is chosen in such a way that $\gamma = \gamma(k_y, k_\parallel)$ takes its maximum value or $\gamma = \max_{k_x} \gamma(k_x, k_y, k_\parallel)$. In Fig. 1(a), where only the parallel diffusion coefficients $\mu_\parallel$ and $\chi_\parallel$ are taken to be finite, growth rate distribution on the $(k_y, k_\parallel)$ plane is more widespread in the k_y-direction than the growth rate in Fig. 1(b). In Fig. 1(b) the perpendicular diffusion coefficients $\mu_\perp$ and $\chi_\perp$ are also taken into account.

B.   Eigenmode Stability Theory

Now we consider the eigenvalue problem in more detail without using the local approximation. The solutions of the linearized equations of the system (5)–(7) with the following forms are considered:

$$\phi = \widetilde{\phi}(\widetilde{x}) \exp i(k\widetilde{y} - \widetilde{\omega}\tau) ,$$

$$v = \widetilde{v}(\widetilde{x}) \exp i(k\widetilde{y} - \widetilde{\omega}\tau) ,$$

$$p = \widetilde{p}(\widetilde{x}) \exp i(k\widetilde{y} - \widetilde{\omega}\tau) ,$$

where $\omega, \widetilde{\phi}(x)$, $\widetilde{v}(x)$ and $\widetilde{p}(x)$ are assumed to take complex values and k denotes the real wavenumber $k = \widetilde{k}_y$. The $\widetilde{z}$-dependence of the solutions is ignored since, in the case of a finite shear s, the $\widetilde{z}$-dependence of the linear solutions only shifts the position of their mode rational surfaces in the x-direction. Assuming that $\mu_\perp = \chi_\perp = 0$ in the system (5)–(7) for simplicity, the linearized equations of this system are reduced to the following eigenvalue

problem

$$\frac{d^2}{d\widetilde{x}^2}\widetilde{\phi} + \left(-k^2 + \frac{1-\Omega}{\Omega+K} + \frac{B+K}{\Omega+K}\cdot\frac{s^2\widetilde{x}^2}{AB-s^2\widetilde{x}^2\Gamma}\right)\widetilde{\phi} = 0 \ , \tag{19}$$

where

$$A = \Omega + i\mu_{\parallel}k\,s^2\widetilde{x}^2$$

$$B = \Omega + i\chi_{\parallel}k\,s^2\widetilde{x}^2$$

and $\Omega = \widetilde{\omega}/k = \omega/\omega_e^*$. The relations of $\widetilde{v}$ and $\widetilde{p}$ to $\widetilde{\phi}$ are given by

$$\widetilde{v} = \frac{s\widetilde{x}(K+B)}{AB-s^2\widetilde{x}^2\Gamma}\,\widetilde{\phi}$$

and

$$\widetilde{p} = \frac{AK+s^2\,\widetilde{x}\Gamma}{AB-s^2\,\widetilde{x}^2\Gamma}\,\widetilde{\phi} \ .$$

In this subsection B, we only consider an ideal sheared slab or $L_x = \infty$. As discussed in Sec. II, therefore, the boundary condition of Eq. (19) is such that $|\widetilde{\phi}(x)| \to 0$ as $|\widetilde{x}| \to \infty$.

It is known[4] that, in the case where $\mu_{\parallel} = \chi_{\parallel} = \Gamma = 0$, Eq. (19) gives the following eigenvalue Ω and the eigenfunction ϕ:

$$\Omega = \frac{1}{2(1+k^2)}\left[\left(1-k^2K-is(2\ell+1)\right)\pm\sqrt{\left(1-k^2K-is(2\ell+1)\right)^2-4is(1+k^2)(2\ell+1)K}\,\right] \tag{20}$$

and

$$\widetilde{\phi} = e^{-\sigma\widetilde{x}^2/2}H_\ell(\sigma^{1/2}\,\widetilde{x}) \ , \tag{21}$$

where $\sigma = is/\Omega$, ℓ $(\ell \geq 0)$ is the radial mode number associated with the ℓth eigenvalue of Weber equation, and $H_\ell(z)$ is the ℓth-order Hermitian function of the complex variable z.

Since the shear parameter s is generally a small number, we are able to reduce the expression of Ω of Eq. (20) to somewhat simpler forms in the following two limiting case.

14

First we consider the case where

$$\left| \tilde{s}/(1 - k^2 K) \right| \ll 1 \tag{22}$$

with $\tilde{s} = (2\ell + 1)s$. Although we do not take any specific ordering of k^2, the condition above is in practice satisfied when $|k^2 K| \ll 1$, so we assume $1 - k^2 K > 0$ under this condition. We note that the mode under consideration is not the fastest growing mode. We also note that, in the local approximation, the condition (22) causes the balance between the second term and the third term of Eq. (14) or, in other words, strong coupling of the drift wave with the ion acoustic wave. In this case, the term given as the square root in the right-hand side of Eq. (20) is analytic at $s = 0$. Therefore we expand Ω in terms of $\varepsilon_1 = \tilde{s}/(1 - k^2 K)$ around $\varepsilon_1 = 0$. Taking up to the third order of ε_1, we obtain

$$\mathrm{Re}\,\Omega = -K \left(1 + \frac{1 + k^2}{1 - k^2 K} K \right) \left(\frac{(2\ell + 1)s}{1 - k^2 K} \right)^2 + \mathcal{O}\left(\varepsilon_1^4 \right) \tag{23}$$

and

$$\mathrm{Im}\,\Omega = \frac{(2\ell + 1)sK}{1 - k^2 K} - K \left(1 + 2\frac{1 + k^2}{1 - k^2 K} K \right) \left(1 + \frac{1 + k^2}{1 - k^2 K} \right) \left(\frac{(2\ell + 1)s}{1 - k^2 K} \right)^3$$
$$+ \mathcal{O}(\varepsilon_1^5) . \tag{24}$$

A stabilizing effect of a larger shear s, appears as the $\mathcal{O}(\varepsilon_1^3)$ correction in Eq. (24). It follows from Eqs. (23) and (24) that, to the lowest order in ε_1, the fundamental mode ($\ell = 0$) with a small wavenumber k is a purely growing mode with the complex eigenfrequency

$$\Omega = i\,sK \tag{25}$$

or $\omega = -i\,\omega_{pi}^* s$ $\quad (\omega_{pi}^* < 0)$.

The maximum growth rate is, however, attained when $|1 - k^2 K| \ll 1$, as also seen in the local analysis. Unlike the condition (22), under the condition

$$|1 - k^2 K| \lesssim |\tilde{s}| \ll 1 , \tag{26}$$

15

the square root term of the right-hand side of Eq. (20) is no longer analytic at $s = 0$. We therefore expand the square root term in terms of $(1 - k^2 K + i\widetilde{s})^2 / i\widetilde{s}(K + 1)$ and obtain both maximum $\mathrm{Im}\,\Omega$ and maximum growth rate $\widetilde{\gamma}$,

$$\mathrm{Im}\,\Omega = \frac{K}{2}\left(\sqrt{\frac{2(2\ell + 1)s}{K + 1}} - \frac{(2\ell + 1)s}{K + 1} + \mathcal{O}\left(\varepsilon_2^{3/2}\right)\right) \tag{27}$$

$$\widetilde{\gamma} = k\,\mathrm{Im}\,\Omega = \frac{\sqrt{K}}{2}\left(\sqrt{\frac{2(2\ell + 1)s}{K + 1}} - \frac{(2\ell + 1)s}{K + 1} + \mathcal{O}\left(\varepsilon_2^{3/2}\right)\right) \tag{28}$$

at

$$k^2 = \frac{1}{K} + \mathcal{O}(\varepsilon_2) \ . \tag{29}$$

The real frequency at this wavenumber k is given by

$$\mathrm{Re}\,\Omega = \frac{K}{2}\left(-\sqrt{\frac{2(2\ell + 1)s}{K + 1}} - \frac{3(2\ell + 1)s}{K + 1} + \mathcal{O}\left(\varepsilon_2^{3/2}\right)\right) \ . \tag{30}$$

Here $\varepsilon_2 = (2\ell + 1)s/(K + 1)$. For the fundamental mode ($\ell = 0$) with large K, we obtain the familiar formulas[4]

$$\mathrm{Im}\,\Omega \simeq \sqrt{sK/2}$$

$$\text{and} \qquad \mathrm{Re}\,\Omega \simeq -\sqrt{sK/2} \tag{31}$$

to the lowest order of s. In the dimensional form, the complex eigenfrequency is given by $\omega = (-1 + i)\sqrt{s/2}\,(c_s/L_n)$, i.e., independent of K to the lowest order of s. Under the condition (26) the instability obtained here is more due to the balance between the first term and the third term of Eq. (14) or the destabilization of the ion acoustic wave by the thermal mode, rather than the coupling of the drift wave with the destabilized ion acoustic wave.

So far we have considered the case where the radial number ℓ is small enough so that either Eq. (22) or Eq. (26) holds. However, as shown in Eqs. (24) and (27), larger radial eigenmode number ℓ tends to increase the growth rate when the shear s is small. Since the

16

dependence of Ω in Eq. (20) on ℓ is given by its dependence on $\tilde{s} = (2\ell + 1)s$, we plot the growth rate $\gamma = \mathrm{Im}\,\tilde{\omega} = k\,\mathrm{Im}\,\Omega$ as a function of $\tilde{s}$ and k in Fig. 2. Here $k = 0.2m$ and $K = 3.0$. The maximum of $\gamma_{\mathrm{max}} = 0.753$ is obtained at $\tilde{s} = \tilde{s}_{\mathrm{max}} = 0.75$ and $k = 1.4$ (or $m = 7$). As a function of small shear s ($s \ll 1$), the growth rate γ remains constant at its maximum γ_{max} since, as s (not $\tilde{s}$) decreases, the radial eigenmode number ℓ increases so as to keep $\tilde{s} = (2\ell + 1)s$ at the constant value $s = \tilde{s}_{\mathrm{max}}$. Figure 3 shows the dependence of γ on s (not $\tilde{s}$) calculated from Eq. (20) when $K = 3.0$. Here ℓ and m (or k) are chosen to maximize the growth rate γ. It is shown that the $\ell = 0$ mode is dominant when $s \geq 4.1$ and the $\ell = 1$ mode is dominant when $1.8 \leq s \leq 4.1$. For $s = 0.1$, which is a typical shear parameter of a tokamak plasma, the radial eigenmode number is given by $\ell = 38$ when $K = 3$. We note that this unrealistically high radial eigenmode number ℓ is reduced when the effect of finite Γ and finite diffusion are taken into account, as will be shown later.

Returning to the original eigenvalue problem of Eq. (19), we now seek the stabilizing effects of the compressibility of the parallel flow (i.e., $\Gamma \neq 0$) and the parallel diffusion (i.e., $\mu_{\parallel}, \chi_{\parallel} \neq 0$). It should be noted that by using non-zero values of $\mu_{\parallel}$ and $\chi_{\parallel}$, we are able to avoid the singularity of the last term of Eq. (19) arising from the finite value of Γ. Assuming that $s^2\Gamma$, $|\mu_{\parallel}ks^2|$ and $|\chi_{\parallel}ks^2|$ are small, we expand the last term of the left-hand side of Eq. (19) as Taylor series in x. Here we also assume that the mode is localized near $x = 0$, or more precisely, we solve Eq. (19) on a finite domain of x ($|x| \leq L_x$) with the boundary conditions that $|\tilde{\phi}| = 0$ at $|x| = L_x$. Therefore, by taking the values of $s^2\Gamma$, $|\mu_{\parallel}ks^2|$ and $|\chi_{\parallel}ks^2|$ to be small enough, the Taylor expansion is uniformly convergent. The size of the domain L_x, however, is taken to be large enough, so that the lowest order solution of Eq. (19) is well approximated by Eq. (21) with the eigenvalue Eq. (20).

Writing Ω as the sum of the lowest order growth rate Ω_0 given by the right-hand side of Eq. (20) and the remainder Ω_1, where $|\Omega_1/\Omega_0|$ is also assumed to be small, we expand

17

Eq. (19) in terms of these small parameters. Retaining up to the term of $\tilde{x}^4$, we obtain

$$\frac{d^2\tilde{\phi}}{d\tilde{x}^2} + (E_0 + E_1 - V_0(\tilde{x}) - V_1(\tilde{x}))\,\tilde{\phi} = 0 \;, \tag{32}$$

where

$$E_0 = -k^2 + \frac{1 - \Omega_0}{\Omega_0 + K}\;,$$

$$E_1 = -\frac{K+1}{(\Omega_0 + K)^2}\,\Omega_1 \;, \tag{33}$$

$$V_0 = -\frac{s^2\tilde{x}^2}{\Omega_0^2}\;,$$

$$V_1 = \frac{1}{\Omega_0^2}\left(\frac{2\Omega_1}{\Omega_0}\,s^2\tilde{x}^2 - Ds^4\,\tilde{x}^4\right)\;,$$

and

$$D = \frac{\Gamma}{\Omega_0^2} - \frac{i(\mu_\parallel + \chi_\parallel)k}{\Omega_0} + \frac{i\chi_\parallel k}{\Omega_0 + K}\;.$$

To the lowest order, Eq. (32) becomes Eq. (19) or

$$\frac{d^2\tilde{\phi}_0}{dx^2} + (E_0 - V_0(x))\,\tilde{\phi}_0 = 0 \;, \tag{34}$$

where we expand $\tilde{\phi}$ as

$$\tilde{\phi} = \tilde{\phi}_0 + \tilde{\phi}_1 + \cdots \;. \tag{35}$$

The ℓth eigenvalue $\Omega_0 = \Omega_0^{(\ell)}$ and the ℓth eigenfunction $\tilde{\phi}_0 = \tilde{\phi}_0^{(\ell)}$ of Eq. (34) are given by Eqs. (20) and (21), respectively. From the next order equation and using the solvability condition of the inhomogeneous equation, we obtain the following relation,

$$E_1 = \int_{-\infty}^{\infty} V_1(\tilde{x})\phi_0^{(\ell)2}d\tilde{x}\bigg/ \int_{-\infty}^{\infty} \phi_0^{(\ell)2}d\tilde{x} \;, \tag{36}$$

where the integral is taken over the total domain (i.e., $|\tilde{x}| \leq L_x$ in the case of the finite domain). Using Eq. (21) as $\phi_0^{(\ell)}$, we rewrite Eq. (36) as

$$E_1 = -D\frac{s^4}{\Omega_0^2\sigma_2}\,A_\ell + \frac{2s^2\Omega_1}{\Omega_0^3\sigma}\,B_\ell \;, \tag{37}$$

18

where

$$A_\ell = \int_{-\infty}^{\infty} \xi^4 \, e^{-\xi^2} H_\ell^2(\xi) d\xi \Big/ \sqrt{\pi} \, 2^\ell \ell! = \frac{3}{4} \left(2\ell^2 + 2\ell + 1\right)$$

and

$$B_\ell = \int_{-\infty}^{\infty} \xi^2 \, e^{-\xi^2} H_\ell^2(\xi) d\xi \Big/ \sqrt{\pi} \, 2^\ell \ell! = \frac{1}{2} \left(2\ell + 1\right) .$$

Equating Eq. (33) and (37) and solving the resulting equation for Ω_1 yields

$$\Omega_1^{(\ell)} = -s^2 D \, A_\ell \left(\frac{K+1}{(\Omega_0 + K)^2} - 2i \, \frac{s \, B_\ell}{\Omega_0^2} \right)^{-1} , \qquad (38)$$

which is the first order correction to the ℓth eigenvalue $\Omega_0^{(\ell)}$.

In order to observe the stabilizing effects arising from finite values of $\mu_\parallel$, $\chi_\parallel$ and Γ, we further simplify Eq. (38) under the assumption (22) or $|\varepsilon_1| \ll 1$. Since Eq. (38) gives a $|s|^2$ order correction to the unperturbed eigenvalue $\Omega_0^{(\ell)}$, we need the expression of $\mathrm{Im}\,\Omega_0^{(\ell)}$ correct up to $\mathcal{O}(\varepsilon_1^2)$;

$$\mathrm{Im}\,\Omega_0^{(\ell)} = \frac{(2\ell+1)sK}{1 - k^2 K} + \mathcal{O}(\varepsilon_1^3) .$$

Substituting this expression to Eq. (38) and keeping the terms up to $\mathcal{O}(\varepsilon_1^2)$, Eq. (38) becomes

$$\mathrm{Re}\,\Omega_1^{(\ell)} = \frac{3}{4} \left(2\ell^2 + 2\ell + 1\right) \frac{(K+1)\Gamma s^2}{(1 - k^2 K)^2} + \mathcal{O}(\varepsilon_1^3)$$

and

$$\mathrm{Im}\,\Omega_1^{(\ell)} = -\frac{3(2\ell^2 + 2\ell + 1)}{4(2\ell + 1)} s \left(\Gamma + k(\mu_\parallel + \chi_\parallel) \frac{(2\ell+1)Ks}{1 - k^2 K} \right) + \mathcal{O}(\varepsilon_1^3) .$$

Therefore the growth rate of the mode $\mathrm{Im}\,\Omega^{(\ell)} = \mathrm{Im}\,\Omega_0^{(\ell)} + \mathrm{Im}\,\Omega_1^{(\ell)}$ is given to $\mathcal{O}(\varepsilon_1^2)$ by

$$\mathrm{Im}\,\Omega^{(\ell)} = (2\ell+1)s \left(\frac{K}{1 - k^2 K} - \frac{3}{4} \cdot \frac{(2\ell^2 + 2\ell + 1)}{(2\ell + 1)^2} \left(\Gamma + k(\mu_\parallel + \chi_\parallel) \frac{(2\ell+1)Ks}{1 - k^2 K} \right) \right) . \qquad (39)$$

It follows that in the case of $\ell = 0$ and small k^2, Eq. (39) is reduced to

$$\mathrm{Im}\,\Omega^{(0)} = s \left(K - \frac{3}{4} \Gamma - \frac{3}{4} k(\mu_\parallel + \chi_\parallel) K \, s \right) \qquad (40)$$

19

to the lowest order in k^2. We thus find from Eq. (40) that the growth rate is reduced by the compressibility of the parallel flow (i.e., nonzero Γ) and parallel diffusions (i.e., nonzero $\mu_\parallel$ and $\chi_\parallel$). We, however, note that Eqs. (39) and (40) are valid only for a specific k that may vary in the small range $0 \leq k^2 \ll 1/K$. Therefore, the expressions of the growth rate given in these equations do not represent the general k-dependence of the growth rate. We also note that the radial eigenmode number ℓ and the wavenumber k are fixed in the above calculations. Figures 4(a) and (b) show $\mathrm{Im}\,\Omega$ of Eq. (40) as a function of K and s, respectively, and compare this analytic expression to the exact eigenvalue $\mathrm{Im}\,\Omega$ obtained from a shooting code, solving Eq. (19).

Although Eqs. (39) and (40) are derived under the assumption that the stabilizing terms associated with Γ, $\mu_\parallel$ and $\chi_\parallel$ be small, we extrapolate the result to the case where the second and third terms in the parentheses of Eq. (40) are comparable to the first term K in order to estimate the critical value $K_c^{(0)}(k)$ of K for a given small wavenumber k. Setting $\mathrm{Im}\,\Omega^{(0)} = 0$ in Eq. (40), the critical value $K_c^{(0)}(k)$ is approximately given by

$$K_c^{(0)}(k) = \frac{3}{4}\,\Gamma\left(1 + \frac{3}{4}\,k(\mu_\parallel + \chi_\parallel)s\right) \, , \qquad (41)$$

or, in terms of η_i, the equation above may be rewritten as

$$\eta_{i,c}^{(0)}(k_y\rho_s) = \frac{3}{4}\,\gamma - 1 + \frac{9}{16}\,\gamma\,\frac{(\nu_\parallel + \kappa_\parallel)}{c_s L_n}\,k_y\,\rho_s\left(\frac{L_n}{L_s}\right) \, . \qquad (42)$$

Here $\nu_\parallel$ and $\kappa_\parallel$ are the parallel viscosity and the parallel heat conductivity in the dimensional form, defined by $\nu_\parallel = m_i n_0\,c_s L_n\,\mu_\parallel$ and $\kappa_\parallel = c_s L_n\,\chi_\parallel$, and $T_i = T_e$ is assumed. For example, in the case where $\gamma = 2$, $\mu_\parallel = \chi_\parallel = 2$, $k = k_y\rho_s = 0.5$ and $s = L_n/L_s = 0.3$, we have $\eta_{i,c}^{(0)}(k = 0.5) \simeq 1.2$. The critical value η_i of the mode, denoted by $\eta_{i,c}$, is the minimum value of $\eta_{i,c}^{(\ell)}(k)$ i.e., $\eta_{i,c} = \min_{\ell,k} \eta_{i,c}^{(\ell)}(k)$. As we noted, however, Eqs. (39) and (40) are valid only for a limited range of k and not appropriate to estimate $\eta_{i,c}$. The critical value $\eta_{i,c}$ may be obtained with the use of the unperturbed eigenvalue Ω_0 evaluated near $k = K^{-1/2}$ given in Eqs. (27) and (30) with an appropriate choice of ℓ. However, we do not proceed

to this calculation here since our objective in the perturbation analysis presented here is to demonstrate the stabilizing effects arising from Γ, $\mu_\parallel$, and $\chi_\parallel$, which are shown in Eq. (39).

C.   Mixing Length Estimates

We now estimate the nonlinear saturation level of the η_i-mode turbulence using the linear properties obtained in this section. By means of the mixing length theory, the anomalous diffusion coefficient D is estimated as

$$D = \tilde{\gamma}\, \Delta_x^2 \;, \tag{43}$$

where Δ_x is the typical mode width in the $\tilde{x}$-direction. We here use the following definition of Δ_x

$$\Delta_x^{-2} = \left| \text{Re}\left(\left\langle (\partial\phi/\partial\tilde{x})^2 \right\rangle \Big/ \left\langle \phi^2 \right\rangle \right) \right| \;. \tag{44}$$

For the lowest order solution $\phi = \phi_0$ of Eq. (34), we obtain

$$\Delta_x^{-2} = \left| \text{Re}\left(\lambda - \frac{1}{2}\sigma(2\ell+1) \right) \right| \;, \tag{45}$$

where

$$\lambda = -k^2 + \frac{1-\Omega}{\Omega + K} \;. \tag{46}$$

Choosing the fundamental mode ($\ell = 0$) with a small wavenumber ($|k^2 K| \ll 1$), we estimate the anomalous diffusion coefficient D using Eq. (25) in Eqs. (45) and (46) as

$$D = 2k\, s\, K^2 \tag{47}$$

to the lowest order of s. In this case, the mode width $\Delta_x = \sqrt{2K}$ estimated from Eq. (45) does not depend on the shear s.

If we use, however, the most strongly excited mode to evaluate Eq. (45), we obtain a different scaling of D. To the lowest order of s, the fastest growing mode is obtained when $k \simeq K^{-1/2}$ and $(2\ell+1)s = \tilde{s}_{\text{max}}$, the growth rate of which is given by Eqs. (27) or

21

$\mathrm{Im}\,\Omega \simeq \sqrt{(2\ell+1)s\,K/2}$ if K is large. Here, as before, $\tilde{s}_{\max}$ denotes the value of $\tilde{s} = (2\ell+1)s$ that maximizes $\mathrm{Im}\,\Omega$ given by Eq. (20). With the use of this growth rate, the anomalous mixing length diffusion coefficient D is evaluated by

$$D = 2\sqrt{K}\,, \tag{48}$$

which is independent of the shear s. In this case, the mode width Δ_x of the fastest growing mode is given by

$$\Delta_x^{-2} = \frac{1}{2}\sqrt{\frac{(2\ell+1)s}{2K}} \tag{49}$$

to the lowest order of s. For the fixed radial mode number ℓ, Δ_x scales as $s^{-1/4}$ while with the choice of ℓ such that $(2\ell+1)s = \tilde{s}_{\max}$, Δ_x is independent of shear.

In more realistic cases of finite Γ and finite diffusion, we use the linear initial value code to obtain the growth rate of the fastest growing mode. Figure 5 shows the growth rate $\gamma = k\,\mathrm{Im}\,\Omega$ calculated from the initial value code as a function of the shear s, where $K = 3.0$, $\Gamma = 2$, $\mu_{\parallel} = \chi_{\parallel} = 1.0$ and $\mu_{\perp} = \chi_{\perp} = 0.01$. The linear initial value code used here is the same code as the nonlinear initial value code used in Sec. V except for the nonlinear terms dropped in these calculations. In Fig. 5, it is shown that the growth rate γ is approximately a decreasing function of s in contrast to γ in Fig. 3 which is almost constant when $s \lesssim 1$. Figure 6 shows the anomalous diffusion coefficients D calculated from the mixing length estimate $D = \tilde{\gamma}\,\Delta_x^2$ as a function of s. Here $\tilde{\gamma} = \gamma\,L_n/c_s$ and

$$\Delta_x^{-2} = \left\langle (d\phi/dx)^2 \right\rangle / \left\langle \phi^2 \right\rangle\,,$$

are evaluated by the linear initial value code with the real-valued function ϕ and the same parameters used in Fig. 5. With the effects of finite Γ and finite diffusion, Fig. 6 shows weak dependence of D on s as $D \propto s^{-1/2}$ in contrast to Eq. (48). Taking into account this shear dependence of D forces the modification of Eq. (48) to become

$$D \propto (K/s)^{1/2}\,. \tag{50}$$

22

The previous work by Lee and Diamond[9] reports the scaling of the anomalous ion heat conductivity χ_i essentially identical to Eq. (47) while the previous work by Horton, Estes and Biskamp[7] reports the scaling of χ_i similar to Eq. (50). As shown in this section and also as will be discussed in Sec. VI, the disagreement between these two previous results arises from the choice of the linear mode used to evaluate the nonlinear saturation levels; in Ref. 9, the fundamental mode with small $k_y \rho_s$ (i.e., $\ell = 0$, $|k^2 K| \ll 1$) is taken to be responsible for the nonlinear process while in Ref. 7 the most strongly excited mode is considered to be important. Since the mixing length theory does not provide information about such a-priori choice of linear modes important in the nonlinear process, we need to proceed to more rigorous analyses and numerical simulations.

IV. Nonlinear Theory: Bifurcation Near the Threshold

We now derive the saturation amplitude of the nonlinear η_i-mode and the associated anomalous heat flux as a function of the ion temperature gradient or η_i near its critical value $\eta_{i,c}$. The method used here is the amplitude expansion method,[21,22] in which we regard the non-linearly saturated mode with small amplitude as the bifurcation from a marginally stable state and expand the dynamical equations with respect to the small amplitude around the linear solutions.

For convenience, we rewrite the dynamical equations (5)–(7) as follows:

$$M \frac{\partial}{\partial \tau} \psi + \mathcal{L}(K)\psi + N(\psi, \psi) = 0 , \qquad (51)$$

where

$$\psi = \begin{pmatrix} \phi \\ v \\ p \end{pmatrix}$$

$$\mathcal{L}(K) = L_1 + KL_2 \quad , \quad M = \begin{pmatrix} 1 - \Delta_\perp & 0 & 0 \\ 0 & 1 & 0 \\ 0 & 0 & 1 \end{pmatrix}$$

$$L_1 = \begin{pmatrix} \partial/\partial\tilde{y} + \mu_\perp \nabla_\perp^4 & \nabla_\parallel & 0 \\ \nabla_\parallel & -\mu_\parallel \nabla_\parallel^2 - \mu_\perp \nabla_\perp^2 & \nabla_\parallel \\ 0 & \Gamma\nabla_\parallel & -\chi_\parallel \nabla_\parallel^2 - \chi_\perp \nabla_\perp^2 \end{pmatrix}$$

$$L_2 = \begin{pmatrix} \nabla_\perp^2 \, \partial/\partial\tilde{y} & 0 & 0 \\ 0 & 0 & 0 \\ \partial/\partial y & 0 & 0 \end{pmatrix} \, .$$

The nonlinear vector term $N(\psi, \psi)$ is defined as

$$N(f, g) = \begin{pmatrix} -\{f_1, \nabla_\perp^2 g_1\} \\ \{f_1, g_2\} \\ \{f_1, g_3\} \end{pmatrix}$$

for $f = (f_1, f_2, f_3)^T$ and $g = (g_1, g_2, g_3)^T$, where the superscript T denotes the transpose of the matrix. The linear analysis in Sec. II shows that Eq. (51) generally has a time periodic solution in the zero amplitude limit. We therefore expect that there also exists a time periodic solution at the marginally stable state to the nonlinear system (51), the period of which is generally a function of the amplitude. For a sufficiently small amplitude ε we search for the nonlinear solution ψ of Eq. (51) by expansion in ε. We therefore introduce the new variables

$$\psi = \varepsilon \, u(\mathbf{x}, s)$$
$$s = \omega(\varepsilon)\tau \tag{52}$$

such that u is 2π-periodic in s or $u(\mathbf{x}, s + 2\pi) = u(\mathbf{x}, s)$. Here ε is the amplitude of the mode defined by

$$\varepsilon^2 = \frac{1}{2\pi V} \int_0^{2\pi} ds \int_V d\mathbf{x} |\psi|^2 \, , \tag{53}$$

where $\mathbf{x} = (\tilde{x}, \tilde{y}, \tilde{z})$, V is the total volume of the domain defined in Sec. II and $|\psi|^2 = |\phi|^2 + |v|^2 + |p|^2$. Considering a set of functions $H = \left\{ f(\mathbf{x}, s) = (f_1, f_2, f_3)^T \right\}$, where $f_i =$

$f_i(\mathbf{x}, s)$ $(1 \le i \le 3)$ is 2π periodic in s and satisfies the boundary conditions given in Sec. II (and has appropriate regularities in $(\mathbf{x}, s)$), we define the inner product of $f, g \in H$ as

$$\langle f, g \rangle = \frac{1}{2\pi V} \int_0^{2\pi} ds \int_V d\mathbf{x} \, f \cdot g^* \ .$$

Here g^* denotes the complex conjugate of g and $f \cdot g^* = \sum_i f_i g_i^*$ $(1 \le i \le 3)$. Clearly $u(\mathbf{x}, s)$ defined in Eq. (52) is an element of H. Using Eqs. (51)–(53), we have

$$\omega(\varepsilon) M \frac{\partial u}{\partial s} + \mathcal{L}(K)u + \varepsilon N(u, u) = 0$$

$$\|u\| = 1 \qquad u\epsilon H \ , \tag{54}$$

where $\|u\| = \langle u, u \rangle^{1/2}$. The goal of the analysis in this section is to solve Eq. (54) in the limit of small ε.

In the case of $\varepsilon = 0$, Eq. (54) is reduces to the linear system discussed in Sec. III, the solution of which exists only when K satisfies the dispersion relation, i.e., $K = K_0(\omega)$. We therefore expect that, also for nonzero ε, Eq. (54) has a solution only when K and $\omega(\varepsilon)$ satisfy a certain relation or K is a certain function of ε. Assuming that ω, K and u are analytic functions of ε, we expand them as follows:

$$\begin{aligned} \omega &= \omega_0 + \omega_1 \varepsilon + \omega_2 \varepsilon^2 + \cdots \\ K &= K_0 + K_1 \varepsilon + K_2 \varepsilon^2 + \cdots \\ u &= u_0 + u_1 \varepsilon + u_2 \varepsilon^2 + \cdots \ , \end{aligned} \tag{55}$$

where

$$u_i = \begin{pmatrix} \phi_i \\ v_i \\ p_i \end{pmatrix} \qquad (i \ge 0) \ .$$

Substituting Eqs. (55) to Eq. (54), we obtain the linear equations to the lowest order

$$\mathcal{T} u_0 = 0 \ , \tag{56}$$

$$\|u_0\| = 1 \qquad \text{and} \qquad u_0 \epsilon H \ , \tag{57}$$

where $\mathcal{T} = \omega_0 M \frac{\partial}{\partial s} + \mathcal{L}_0$ and $\mathcal{L}_0 = L_1 + K_0 L_2$. Since we are interested in a saturated state near the marginally stable state, we have

$$\text{Im }\omega_i = 0 \qquad (i \geq 0)$$

and

$$K_0 = K_c \ .$$

It should be noted that, as discussed in Sec. III, the real frequency Re ω_0 does not vanish generally at the marginally stable state, and the growth rate Im ω_0 changes from negative to positive as K passes K_c from below, i.e.,

$$\frac{d(\text{Im }\omega_0)}{dK}\bigg|_{K=K_c} > 0 \ . \tag{58}$$

The two independent solutions of Eq. (56) are given by $u_0 = e^{is}\xi$ and $e^{-is}\xi^*$, where ξ satisfies

$$i\omega_0 M\xi + \mathcal{L}_0\xi = 1 \ . $$
$$\|\xi\| = 1 \ . \tag{59}$$

For simplicity we assume that there is a unique solution ξ of this system at the marginal stable state. Since a real-valued solution of Eq. (56) at the marginally stable state is of our interest, we may choose $u_0 = \text{Re}(e^{is}\xi) = \frac{1}{2}\left(e^{is}\xi + e^{-is}\xi^*\right)$ without loss of generality.

To the next order of ε, we obtain from Eqs. (54) and (55)

$$\mathcal{T} u_1 = b \ , \tag{60}$$

where

$$b = -\omega_1 M \frac{\partial u_0}{\partial s} - K_1 L_2 u_0 - N(u_0, u_0) \ ,$$

$$\langle u_1, u_0 \rangle = 0 \qquad \text{and} \qquad u_1 \epsilon H \ .$$

In order to write the solvability condition of Eq. (59), we need the solutions $u^\dagger$ of the equation

$$\mathcal{T}^\dagger u^\dagger = 0 \ , \tag{61}$$

26

where $\mathcal{T}^\dagger$ is the adjoint operator of $\mathcal{T}$. Since M is a Hermitian operator, $\mathcal{T}^\dagger$ is given by

$$\mathcal{T}^\dagger = -\omega_0 \, M \, \frac{\partial}{\partial s} + \mathcal{L}_0^\dagger \, ,$$

where $\mathcal{L}_0^\dagger$ is the adjoint operator of $\mathcal{L}_0$. The two independent solutions of (60) are given by $e^{is} \, \xi^\dagger$ and $e^{-is} \, \xi^\dagger$ where $\xi^\dagger$ satisfies

$$-i\omega_0 \, M \, \xi^\dagger + \mathcal{L}_0^\dagger \, \xi^\dagger = 0 \, .$$

Writing the two solutions $u_{(1)}^\dagger = e^{is} \, \xi^\dagger$ and $u_{(2)}^\dagger = e^{-is} \xi^{*\dagger}$, the solvability condition of Eq. (60) is

$$\left\langle u_{(i)}^\dagger, b \right\rangle = 0 \qquad (i = 1, 2) \, . \tag{62}$$

From the s-dependence of the term $N(v_0, v_0)$, it is easy to show that

$$\left\langle u_{(i)}^\dagger, N(u_0, u_0) \right\rangle = 0 \qquad (i = 1, 2) \, .$$

Therefore Eq. (61) becomes

$$\left\langle u_{(i)}^\dagger, \omega_1 \, M \, \frac{\partial}{\partial s} u_0 + K_1 \, L_2 \, u_0 \right\rangle = 0 \qquad (i = 1, 2) \, , \tag{63}$$

which determines ω_1 and K_1. Writing Eq. (63) in terms of ξ, we obtain

$$i\omega_1 \left\langle \xi^\dagger, M \, \xi \right\rangle + K_1 \left\langle \xi^\dagger, L_2 \, \xi \right\rangle = 0 \tag{64}$$

and its complex conjugate. Since the solution ξ of Eq. (59) exists only when ω_0 satisfies the dispersion relation with K i.e., $\omega_0 = \omega_0(K)$ for the parameter K, differentiating Eq. (59) in terms of K yields

$$\left(i \, \frac{d\omega_0}{dK} \, M + L_2 \right) \xi + (i\omega_0 \, M + \mathcal{L}_0) \, \frac{d\xi}{dK} = 0 \, . \tag{65}$$

Evaluating Eq. (63) at $K = K_c$ and taking the inner product of $\xi^\dagger$ and Eq. (65), we obtain

$$i \left(\frac{d\omega_0}{dK} \right)_{K=K_c} \left\langle \xi^\dagger, M \, \xi \right\rangle + \left\langle \xi^\dagger, L_2 \, \xi \right\rangle = 0 \, , \tag{66}$$

where we used

$$\left\langle \xi^\dagger, (i\omega_0 M + \mathcal{L}_0) \frac{d\xi}{dK} \right\rangle = \left\langle \frac{d\xi}{dK}, \left(-i\omega_0 M + \mathcal{L}_0^\dagger\right) \xi^\dagger \right\rangle = 0 \ .$$

From Eqs. (64) and (66), we obtain

$$\left(\omega_1 - K_1 \left(\frac{d\omega_0}{dK}\right)_{K=K_c}\right) \left\langle \xi^\dagger, M \xi \right\rangle = 0 \ . \tag{67}$$

Since $\left\langle \xi^\dagger, M \xi \right\rangle \neq 0$ and ω_1 is a real number, it follows from Eqs. (58) and (67) that

$$\omega_1 = K_1 = 0 \ .$$

To the order of ε^2, we derive from Eqs. (54) and (55)

$$\mathcal{T} u_2 = -\omega_2 M \frac{\partial}{\partial s} u_0 - K_2 L_2 u_0 - F_2 \ , \tag{68}$$

where

$$F_2 = N(u_0, u_1) + N(u_1, u_0) \ .$$

The solvability condition of Eq. (68) then becomes

$$\omega_2 \left\langle u_{(i)}^\dagger, M \frac{\partial u_0}{\partial s} \right\rangle + K_2 \left\langle u_{(i)}^\dagger, L_2 u_0 \right\rangle + \left\langle u_1^\dagger, F_2 \right\rangle = 0 \ ,$$

which may be further reduced to

$$i \left(\omega_2 - K_2 \left(\frac{d\omega_0}{dK}\right)_{K=K_c}\right) \left\langle \xi^\dagger, M \xi \right\rangle + 2 \left\langle u_{(1)}^\dagger, F_2 \right\rangle = 0$$

and its complex conjugate, where we used Eq. (66). Separating this equation into the real and complex parts, we obtain

$$K_2 = -\operatorname{Re}\left(\frac{2 \left\langle u_{(1)}^\dagger, F_2 \right\rangle}{\left\langle \xi^\dagger, M \xi \right\rangle}\right) \Big/ \left[\frac{d(\operatorname{Im} \omega_0)}{dK}\right]_{K=K_c}$$

and

$$\omega_2 = K_2 \left[\frac{d(\operatorname{Re} \omega_0)}{dK}\right]_{K=K_c} - \operatorname{Im}\left(\frac{2 \left\langle u_{(1)}^\dagger, F_2 \right\rangle}{\left\langle \xi^\dagger, M \xi \right\rangle}\right) \ .$$

28

Using K_2 obtained above and the linear marginally-stable solutions, we calculate the anomalous heat flux $\langle p \, \partial\phi/\partial y \rangle$ to its lowest order. Assuming that $K_2 \neq 0$, we have $K - K_c = K_2 \varepsilon^2$ to the lowest order. Therefore,

$$\left\langle p \, \frac{\partial\phi}{\partial\widetilde{y}} \right\rangle = \varepsilon^2 \left\langle p_0 \, \frac{\partial\phi_0}{\partial\widetilde{y}} \right\rangle = \frac{1}{K_2} \left\langle p_0 \, \frac{\partial\phi_0}{\partial\widetilde{y}} \right\rangle (K - K_c) \,, \qquad (69)$$

where p_0 and ϕ_0 are the linear marginally-stable solutions. We note that the coefficient $\langle p_0 \, \partial\phi_0/\partial\widetilde{y} \rangle / K_2$ of $(K - K_c)$ is a function of K_c and s but does not depend on K.

Thus we have derived the dependence of the anomalous heat flux $\langle p_0 \, \partial\phi_0/\partial\widetilde{y} \rangle$ on the ion pressure gradient K in the limit of small amplitude. The dependence of the anomalous heat flux on the shear parameter s is not clear from Eq. (69) since the linear solutions p_0 and ϕ_0 as well as K_2 are generally complicated functions of s. The shear dependence of the coefficient $\langle p_0 \, \partial\phi_0/\partial\widetilde{y} \rangle$ in Eq. (69) may be obtained by solving the linear equations (56) and (57) numerically. However, we now proceed to direct numerical simulations of Eqs. (5)–(6), rather than studying the shear dependence of Eq. (69) in detail. The numerical simulations of the original dynamical system presented in the next section give the dependence of the anomalous heat flux on the shear s as well as the ion pressure gradient K under much wider range of parameters than the method used in this section and check the validity of the analytical result given in Eq. (69).

V.   Numerical Simulations

In this section we report the results of numerical simulations of the η_i-modes and compare the results with the analytical predictions presented in the previous sections. The initial value code used to solve the nonlinear partial differential equations (5)–(7) is developed from the HIB code.[23,24] In the initial value code, Fourier representation for the $\widetilde{y}$ and $\widetilde{z}$ variables and a finite difference scheme for the $\widetilde{x}$ variable are employed. At each time step the dependent variables are advanced by means of the predictor-corrector method. The

boundary condition is that all the physical variables are periodic in $\tilde{y}$ and $\tilde{z}$ with periods L_y and L_z, respectively, and they vanish at $|\tilde{x}| = L_x$, as discussed in Sec. II. We refer to the (m, n)-mode of the Fourier representation as the mode whose $\tilde{y}$ and $\tilde{z}$-dependence is given by the phase $2\pi(m\tilde{y}/L_y - n\tilde{z}/L_z)$. The wave numbers $\tilde{k}_y$ and $\tilde{k}_z$ are thus given by $\tilde{k}_y = 2\pi m/L_y$ and $\tilde{k}_z = 2\pi n/L_z$. In the 2D calculations of the nonlinear single helicity modes, the $\tilde{z}$-dependence of the mode is ignored and the relation $\nabla_\parallel = s\tilde{x}\,\partial/\partial\tilde{y}$ is used, which induces single helicity modes localized at $\tilde{x} = 0$. In the 3D calculations, the rational surface of the (m, n)-mode is at $\tilde{x} = nL_y/ms\,L_z$ since $\nabla_\parallel \propto (msx/L_y - n/L_z) = (ms/L_y)(x - nL_y/ms\,L_z)$ for the (m, n)-mode. For the initial condition, small perturbations are given to each (m, n)-mode at $\tau = 0$.

The typical parameters used in the simulations are $\mu_\parallel = \chi_\parallel = 1.0$, $\mu_\perp = \chi_\perp = 0.01$ to 0.1, $\Gamma = 2, s = 0$ to 0.3 and $K = 0.4$ to 3.0. As noted in Sec. II, the parallel diffusion parameters $\mu_\parallel$ and $\chi_\parallel$ are chosen so as to model the collisionless ion Landau effect for high temperature plasmas. The perpendicular diffusion coefficients $\mu_\perp$ and $\chi_\perp$, on the other hand, may be taken from the classical collisional transport theory.[11] Using the classical viscosity $\nu_\perp \sim nT_i/\omega_{ci}^2\,\tau_i$ and the classical heat conductivity $\kappa_\perp \sim T_i/m_i\,\omega_{ci}^2\,\tau_i$, the normalized perpendicular diffusion coefficients $\mu_\perp$ and $\chi_\perp$ of Eqs. (5)–(7) are given by

$$\mu_\perp = \frac{\nu_\perp\,L_n}{m_i\,n\,c_s\,\rho^2} \simeq \left(\frac{T_i}{T_e}\right)\frac{L_n}{c_s\,\tau_i}$$

and

$$\chi_\perp = \frac{\kappa_\perp\,L_n}{c_s\,\rho^2} \simeq \left(\frac{T_i}{T_e}\right)\frac{L_n}{c_s\,\tau_i}\ ,$$

where τ_i denotes the ion collision time. For a hydrogen plasma with $L_n = 1\,\mathrm{m}$, $T_i = T_e = 3.5\,\mathrm{keV}$, $n = 6.6 \times 10^{19}\,m^{-3}$ and $Z_{\mathrm{eff}} = 2$, we have $\mu_\perp \sim \chi_\perp \sim 0.012$. The shear parameter s may be related to the safety factor q of a toroidal plasma by $s = -\varepsilon_a\,n\,q'/n'q^2$, where ε_a is the inverse aspect ratio. Therefore, the parameters chosen for the following simulation results are in an appropriate range of the parameter space of current tokamak experiments.

We first present the results of 2D simulations of nonlinear single-helicity modes. The size of the domain used for the 2D simulations is $L_x = 20 \sim 40$ and $L_y = 10\pi$, so that the smallest finite wavenumber k_y of the $m = 1$-mode is given by $k_y\,\rho_s = 0.2$. The equally spaced 150 mesh points in the case of $L_x = 20$ and 300 mesh points in the case of $L_x = 40$ are used for discretization of the interval $-L_x \le \widetilde{x} \le L_x$. We also employ the Fourier components of $0 \le m \le 6 \sim 12$, which is confirmed to give enough resolution of the saturated state. Figure 7 shows the time evolution of the total energy E_T [Eq. (12)] for $K = 3$ and $s = 0.1$, where the saturation of the modes is observed at $\tau \simeq 50$. The contours of constant potential at $\tau = 500$ under the same conditions are shown in Fig.8. The constant potential contours are the streamlines of the $\mathbf{E} \times \mathbf{B}$ flow. For comparison the contours of constant potential at saturation with a larger shear $s = 0.5$ is also shown in Fig. 9. It is observed that the modes are more localized to the rational surface $\widetilde{x} = 0$ in the case of strong shear while the modes are spread over a wide range of $\widetilde{x}$ in Fig. 8 for weak shear. The saturation in the 2D simulations presented in this section is mainly due to the flattening of the mean ion pressure gradient or the quasilinear saturation. Although the background ion pressure gradient K is kept as a constant parameter during each numerical simulation, the $m = n = 0$-mode of the perturbed pressure p evolves to cancel the background ion pressure gradient K, as shown in Fig. 10. Since the system (5)–(7) with the boundary conditions employed here does not have any external heat source nor allow cooling at $|\widetilde{x}| = L_x$, the mean ion pressure gradient cannot be maintained as a constant during the time evolution. Therefore the quasilinear saturation is the intrinsic saturation mechanism in this system.

The anomalous ion heat conductivity χ_i is defined by

$$\chi_i = \frac{\overline{\langle \widetilde{p}_i \, \widetilde{v}_{ir} \rangle}}{-p'_{i0}} = \frac{\rho_s}{L_n} \left(\frac{cT_i}{eB}\right) \overline{\left\langle p \frac{\partial \phi}{\partial y} \right\rangle} \Big/ K \ . \tag{70}$$

Here the time average $\overline{g(t)}$ of a time-dependent function $g(t)$ is defined by

$$\overline{g(t)} = \lim_{T \to \infty} \frac{1}{T} \int_0^T g(t)dt$$

31

and the space average $\langle \quad \rangle$, which is somewhat different from Eq. (10), is defined by

$$\langle \quad \rangle = \frac{1}{\Delta L_y L_z} \int_{-L_x}^{L_x} d\tilde{x} \int_0^{L_y} d\tilde{y} \int_0^{L_z} d\tilde{z} \ . \tag{71}$$

In practice, the time average is taken over a reasonably long time period of T after the saturation is attained. The size of the mode width in the $\tilde{x}$-direction is denoted by Δ and used as a normalization factor of Eq. (71) so that averaged values calculated from Eqs. (70) do not depend on choice of L_x when the modes are localized. In our simulations, the definition of Δ is given as follows; for a function $f(\tilde{x})$ representing a physical quantity averaged over $\tilde{y}$ and $\tilde{z}$, we define

$$I(\tilde{x}) = \begin{cases} 1 & \text{if } |f(\tilde{x})| \geq f_{\text{max}}/10 \\ 0 & \text{if } |f(\tilde{x})| < f_{\text{max}}/10 \ , \end{cases}$$

where f_{max} is the maximum value of $|f(\tilde{x})|$ on $|\tilde{x}| \leq L_x$. Then the mode width Δ is defined by

$$\Delta = \int_{-L_x}^{L_x} I(\tilde{x}) \, d\tilde{x} \ ,$$

which gives a good estimate of the "support" of the localized mode. The fluctuation level of the space-averaged anomalous ion heat conductivity $\chi_i(t) = \langle p_i \tilde{v}_{1r} \rangle / (-p'_{i0})$ is then given by

$$\Delta \chi_i = \left\{ \overline{(\chi_i(t) - \overline{\chi_i})^2} \right\}^{1/2} \ , \tag{72}$$

which is shown by error bars in the following figures for χ_i.

The anomalous ion heat conductivity χ_i calculated from Eq. (70) is shown in Fig. 11 as a function of shear. As expected from the linear analysis of Sec. III, the strong shear stabilization of the mode is observed for $s \gtrsim 0.2$, where χ_i decreases approximately as $\chi_i \propto s^{-2}$. On the other hand, χ_i seems to become an independent function of s as s approaches zero, which agrees with the conjecture based on the mixing length theory discussed in Sec. III. In the intermediate range $0.05 \lesssim s \lesssim 0.2$, which is of practical importance for current tokamak experiments, χ_i is a weakly decreasing function of s given by $\chi_i \propto s^{-\beta}$ with $1/2 \lesssim$

$\beta \lesssim 1$. The shear dependence of χ_i is fond to be well parameterized by $\chi_i = \chi_0 \exp(-\alpha s)$ with $\chi_0 = 5.34 \times 10^{-2}$ and $\alpha = 7.2$ for the entire range of s.

Figure 12 shows the anomalous ion heat conductivity χ_i as a function of $K - K_c = (\eta_i - \eta_{ic}) T_i / T_e$, where $K_c = 0.4$. As $K \to K_c$ or the system approaches the marginally stable state, the dependence of χ_i on K is given by $\chi_i \propto (K - K_c)$, which verifies the result of the nonlinear analysis given in Eq. (69). For larger K, χ_i shows a slight deviation from the linear dependence on $K - K_c$. In Figs. 11 and 12 the magnitude of the numerically obtained $\chi_i / (cT_i/eB)(\rho/L_n)$ is, however, significantly small (order of 10^{-2}) and would have a weak effect on the global transport of confined plasmas. This small magnitude χ_0 is due to the quasilinear saturation mechanism which saturates the modes with small amplitude. In confinement experiments, however, the mean ion pressure gradient is maintained constant for a significant period of time in each discharge since the plasma is continuously heated from some external heat sources and cooled at the edge. This situation, which leads to turbulent saturation rather than quasilinear saturation, is simulated in the 3D calculations presented in the rest of this section. We, however, emphasize the importance of the results of 2D nonlinear simulations presented above despite their small saturation amplitudes for the following two reasons. First, the results presented here are nonlinear solutions of the system (5)-(7) (together with the boundary conditions given in Sec. II), which is widely used as a simple fluid model of the η_i-mode in the literature. We note that this system intrinsically saturates the mode quasilinearly. Secondly, and more importantly, 2D solutions of many nonlinear fluid problems often show a qualitative resemblance to their corresponding 3D (turbulent) solutions. We particularly expect the dependence of χ_i on s and $K - K_c$ shown in Figs. 11 and 12, respectively, to be similar to that of the 3D turbulent system.

We now proceed to the 3D simulations. The size of the domain used throughout the following calculations is given by $L_x = 20$, $L_y = 10\pi$ and $L_z = 7.5\pi$, so that the smallest finite wavenumbers are $k_y \rho_s = 0.2$ and $k_z L_n = 0.286$ and the distance between the two rational

33

surfaces of the $m = 1/n = 0$ mode and the $m = 1/n = 1$ mode in the case of shear $s = 0.1$ is about $13\rho_s$. The equally spaced 150 mesh points are used for descritization of the interval $-L_x \leq \tilde{x} \leq L_x$ and $58 \sim 130$ modes are chosen for the Fourier representation that cover at least all the (m, n) modes having positive linear growth rates. In all the 3D simulations presented in this section, we use the perpendicular diffusion parameters $\mu_\perp = \chi_\perp = 0.1$, which are larger than those used in the 2D simulations presented above. These diffusion coefficients significantly reduce numerical instabilities without requiring higher resolution.

To model the confinement experiments without local quasilinear saturation, we add the following auxiliary heat $q = q(x, \tau)$ to Eq. (7) in order to induce turbulent saturation or the saturation of modes due to the balance between the free-energy source and high-k diffusion, rather than the quasilinear saturation observed in the 2D simulations. Equation (7) then becomes

$$\frac{\partial p}{\partial \tau} = -K \frac{\partial \phi}{\partial y} - \Gamma \nabla v - \{\phi, p\} + q + \chi_\perp \nabla_\perp^2 p + \chi_\| \nabla_\|^2 p \tag{73}$$

where

$$q = \langle \{\phi, p\} \rangle_{m=n=0} = \frac{1}{L_y L_z} \int_0^{L_y} d\tilde{y} \int_0^{L_z} d\tilde{z} \, \{\phi, p\} \, .$$

It now follows that the $m = n = 0$ component $p_{00} = \langle p \rangle_{m=n=0}$ of p satisfies the diffusion equation

$$\frac{\partial p_{00}}{\partial t} = \chi_\perp \nabla_\perp^2 p_{00} \, ,$$

which leads to $p_{00} = 0$ in the steady state. The physical meaning of $q(x)$ is the additional heat which prevents the flattening of the mean-ion pressure gradient (i.e., the sum of the constant background ion pressure gradient K and the $m = n = 0$ component of the perturbed pressure p) by carrying the thermal energy from the region $\tilde{x} < 0$ to the region $\tilde{x} > 0$. Our simulations show that, without the heat $q(x, \tau)$, the flattening of the mean ion pressure gradient occurs even in the multi-helicity calculations. We note that the energy equation

34

(13) still holds for the system (5), (6), and (73) since

$$\langle pq \rangle = \langle p_{00} \, q \rangle = 0 \ .$$

Introducing q in the pressure equation, therefore, does not introduce any additional free energy source or sink to the system but simply readjusts the plasma in such a way that the mean ion pressure gradient remains as constant K in the evolution of time. The artificial heat flux q thus models both the heating mechanism of the core plasma and the cooling mechanism of the edge plasma which maintain a finite mean ion pressure gradient for a significant period of time in a confined plasma. Numerically, adding q to the pressure equation is equivalent to setting $p_{00} = 0$ at each time step.

The turbulent saturation of the total energy E_T is shown in Fig. 13 for $K = 3$ and $s = 0.1$. In this 3D simulation, 130 modes ($0 \leq m \leq 9$ and $-6 \leq n \leq 6$) are included. Figure 14 shows the time evolution of the perpendicular kinetic energy $E_{\perp m,n}$ of a few sampled modes under the same conditions. Here $E_{\perp mn} = \langle |\nabla_\perp \, \phi_{mn}(\tilde{x}, \tilde{y}, \tilde{z}, \tau)|^2 \rangle$ with

$$\phi_{mn}(\tilde{x}, \tilde{y}, \tilde{z}, \tau) = \phi_{mn}^c(\tilde{x}, \tau) \cos \psi_{mn} + \phi_{mn}^s(\tilde{x}, \tau) \sin \psi_{mn}$$

and

$$\psi_{mn} = 2\pi (m\tilde{y}/L_y - n\,\tilde{z}/L_z) \ .$$

In this case, the $m = 4$ modes are the linearly most unstable. However, after saturation, the other modes with $m \leq 4$ also reach the energy levels similar to that of the $m = 4$ modes. Integrating the perpendicular kinetic energy in $\tilde{z}$ or $E_{\perp m} = \sum_n \overline{E}_{\perp mn}$ we show in Fig. 15 the perpendicular kinetic energy spectrum obtained by time-averaging $\sum_n E_{\perp mn}$, over $60 \leq t\,c_s/L_n \leq 100$. It is shown that the $m = 3$ mode ($k_y \, \rho_s = 0.6$) has the peak and the other modes with $m \leq 4$ have also relatively high energy levels. The modes with $m \geq 5$ or $k_y \, \rho_s \geq 1.0$ decays significantly. The constant potential contours at $\tau = 100$ of the simulation are shown in Fig. 16. There are three rational surfaces in this domain, with

one being at $x/\rho_s = 0$ and each being separated by distance about $13\rho_s$. Some convection cells are, however, widespread from the rational surfaces, indicating that strong nonlinear interaction is taking place.

The dependence of the anomalous ion heat conductivity χ_i on the shear s obtained from the 3D simulations is shown in Fig. 17 for $K = 3.0$. Comparing Fig. 17 to Fig. 11, we now find that $\chi_i = \chi_0 \exp(-\alpha s)$ with $\chi_0 = 1.58$ and $\alpha = 3.7$. The peak of χ_i as a function of s is obtained at $s = 0$ as expected from the mixing length estimates (Sec. III) and from the 2D simulations. In 3D, however, the magnitude of χ_i is significantly larger than that of the quasilinearly saturated single-helicity modes shown in Fig. 11. Figure 18 shows the dependence of χ_i on $K - K_c = (\eta_i - \eta_c)T_i/T_e$, obtained from the 3D simulations for $s = 0.1$ and $K_c = 1.3$. As in the case of Fig. 12, χ_i is almost linear in $(K - K_c)$ although the χ_i deviates from the linear dependence when $K - K_c$ is small. This is due to transition or successive bifurcation[21] from the coherent nonlinear modes near the marginally stable state $(K \simeq K_c)$ to turbulence $(K \gg K_c)$.

Summarizing the analyses in Secs. III and IV and the numerical results in this section, we obtain the scaling of the anomalous ion heat transport given by

$$\chi_i = g \frac{\rho_s}{L_n} \left(\frac{cT_e}{eB}\right)(K - K_c)e^{-\alpha s} = g \frac{\rho_s}{L_n} \left(\frac{cT_i}{eB}\right)(\eta_i - \eta_{ic})e^{-\alpha s}. \tag{74}$$

As suggested by the mixing length formula (Eq. (50)), the numerical simulations shown in Figs. 11 and 17 and the numerical results in Ref. 4, χ_i seems to scale as $\chi_i \propto s^{-1/2}$ near $s = 0.1$. Taking this into account, we obtain $\alpha \simeq 5$ since $e^{-5s} \simeq 0.2\,s^{-1/2}$ numerically near $s = 0.1$. From the magnitudes of χ_i presented in Figs. 17 and 18, the constant g is of order unity when turbulent saturation occurs. Equation (74) with $g = \mathcal{O}(1)$ and $\alpha \simeq 5$ thus gives the scaling of χ_i in a wide range of the parameter space.

VI. Discussion and Conclusions

We have analyzed the nonlinear ion temperature gradient driven mode or η_i-mode of the sheared slab model based on rigorous analyses and numerical simulations of the reduced fluid Eqs. (5)–(7). A new formula for the anomalous ion heat conductivity due to the η_i-mode turbulence is derived, which differs significantly from some of the previously reported results.[8-10]. It is found from the linear analysis that the finite magnetic shear s has the stabilizing effect reducing the growth rate of the fastest growing linear η_i-mode as the shear s becomes larger. Consequently, the fluctuation levels and the associated anomalous ion heat conductivity χ_i are decreasing functions of the shear s.

It is also shown with the use of the amplitude expansion method[21] that χ_i depends on $(\eta_i - \eta_{i,c})$ linearly near the marginally stable state. The theoretical dependence of χ_i on $(\eta_i - \eta_{i,c})$ is confirmed numerically in the fully developed turbulent state. Numerical simulations demonstrate the turbulent saturation of the η_i-mode, as well as the quasilinear saturation under certain conditions, and confirm the analytically predicted results. A good parametrization summarizing the analytic and numerical results for the anomalous ion heat conductivity $\chi_i(s, \eta_i)$ is given by

$$\chi_i = g \frac{\rho_s}{L_n} \left(\frac{cT_i}{eB} \right) (\eta_i - \eta_{i,c}) \exp(-\alpha s) , \tag{75}$$

where $\alpha \simeq 5$ and $g = \mathcal{O}(1)$. For typical plasma parameters of the TFTR supershot[3] at the half-minor radius, the formula (75) gives $\chi_i = 5.1 \, m^2/s$, where $T_i = 10 \, \text{KeV}$, $B = 4.6 \, \text{T}$, $\rho_s = 1.2 \times 10^{-3} \, m$, $L_n = 0.52 \, m$, $\eta_i = 2.7$, $\eta_{i,c} = 1$ and $s = 0.1$ are used. This gives a comparable magnitude of the ion heat conductivity measured in the experiments.[3]

Horton, Estes and Biskamp obtained[7]

$$\chi_i = g \frac{\rho_s}{L_n} \left(\frac{cT_i}{eB} \right) \frac{(1 + \eta_i)^{1/2+\varepsilon}}{s^{1/2}} \tag{76}$$

basically from numerical simulations of the system (5)–(7) giving $g \simeq 0.3$ and $|\varepsilon| \lesssim 0.5$. The

37

numerical code used in Ref. 7 employs a finite difference method in x, y and z with up-wind derivatives in the $\mathbf{E} \times \mathbf{B}$ convection, which is a different algorithm from the one used in the present work. Considering the fact that $e^{-5s} \simeq 0.2\,s^{-1/2}$ numerically near $s = 0.1$ and taking $\varepsilon = 0.5$, the χ_i-scaling of Eq. (76) is somewhat similar to Eq. (75). However, the scaling of Eq. (75) obtained in the present work represents χ_i under a much wider range of the shear parameter s. We also note that the χ_i-scaling of Eq. (75) has an explicit dependence on the critical ion temperature gradient $\eta_{i,c}$ that is missed by the incompressible theory formulas varying as $(1 + \eta_i)^\beta$.

Some of the previously reported scalings of the anomalous ion heat conductivity[8–10] χ_i significantly differ from Eq. (75), although they are reported to be based on the same system of equations (5)–(7). The main difference between these previously reported scaling and Eq. (75) is the shear dependence of χ_i: in Refs. 8–10, χ_i is asserted to be an increasing function of the shear s and χ_i vanishes as $s \to 0$. Also the scalings of χ_i derived in those references have a different dependence on $K = (1 + \eta_i)T_i/T_e$. In order to clarify what leads to this contradiction between the previously reported results and the new result derived in the present work, we here present brief critiques to Refs. 8–10.

A. Critiques of Earlier Theories

The difference between the results of Refs. 8–10, and from Eq. (75) essentially originates from the inconsistent treatment of the linear properties of the η_i-mode in Refs. 8–10, not from the nonlinear analyses. The problem arises either from oversimplification of the nonlinear system that leads to a system having qualitatively different linear properties or from the ad-hoc choice of "typical" linear properties on which the nonlinear analyses of the mode is based. To make this point clearer, we here repeat three important linear properties of the η_i-mode in Eqs. (5)–(7), which seem not to be given sufficient attention in the previous works.

38

(1) The fastest growing linear mode occurs when the wavenumber is chosen in such a way that the drift wave source term $(1 + K\nabla_\perp^2)$ in the right-hand side of Eq. (5) (or the second term in the left-hand side of Eq. (14)) becomes small, i.e., $k_y\rho_s \simeq K^{-1/2}$. Since the case where $K = (1+\eta_i)T_i/T_e = \mathcal{O}(1)$ is of most interest, it is important to realize that, as long as the system (5)–(7) is concerned, the modes with $k_y\rho_s = \mathcal{O}(1)$ play an important role in the nonlinear system. In reality, the dynamics of such modes may be modified by kinetic effects[6,25,26] to some extent, but this is another question.

(2) The largest growth rate γ of the η_i-mode spectrum is a *decreasing* function of the magnetic shear s and γ approaches its maximum value as $s \to 0$, although the shear dependence of γ is weak when $s \ll 1$. This shear dependence is due to the fact that the radial eigenmode number ℓ that gives the largest growth rate increases as s decreases, so as to keep $\tilde{s} = (2\ell+1)s$ approximately constant. It may be, therefore, misleading to state that the shear dependence of the growth rate $\mathrm{Im}\,\Omega$ is given by $\mathrm{Im}\,\Omega \propto (2\ell+1)s\,K$ when $k_y^2\rho_s^2\,K \ll 1$ and by $\mathrm{Im}\,\Omega \propto \sqrt{(2\ell+1)s\,K}$ when $k_y^2\rho_s^2\,K \simeq 1$. We must understand that the radial mode number ℓ giving the largest growth rate is also a function of the shear s.

(3) There is the shear stabilization effect reducing the linear growth rate for larger shear $s \gtrsim 0.1$. This stabilization effect is due to the compression of the parallel velocity field and to parallel diffusion.

Keeping these linear properties of the η_i-mode in mind, we proceed to critiques of the previous works.

(A) The work by Connor [Ref. 8]

Connor derived the formula of the anomalous heat conductivity

$$\chi_i = g\,\frac{\rho_s}{L_n}\left(\frac{cT_e}{eB}\right) K^{3/2}\,s \tag{77}$$

in the limit of $s\,K \ll 1$ (Eq. (44) in Ref. 8), where g is a constant. In deriving Eq. (77), the following terms are dropped from the system (5)–(7) as ignorable; the parallel compression

39

$\Gamma p \nabla_\parallel v$, the inertia of the vorticity $(1 - \nabla_\perp^2)\partial\phi/\partial\tau$ and the parallel electric field $-\nabla_\parallel \phi$. No diffusion terms are included, either, which we, however, do not question at this point since it is generally considered that the turbulent states have a weak dependence on the diffusion coefficients. Inclusion of the nonlinearity due to the finite Larmor radius effect or $\{\partial p/\partial x, \partial\phi/\partial x\} + \{\partial p/\partial y, \partial\phi/\partial y\}$ in the vorticity equation (Eq. (35) of Ref. 8) does not change the argument presented here. Dropping the parallel compression $\Gamma p \nabla_\parallel v$, the inertia of the vorticity due to the polarization drift $-\nabla_\perp \partial\phi/\partial\tau$ and the parallel electric field $-\nabla_\parallel \phi$ causes, in fact, less significant problems. After ignoring these three linear terms from the system (5)–(7), the linear eigenvalue is now given by the following quadratic equation

$$\Omega^2 - (1 - \tilde{k}^2 K)\Omega + i\tilde{s} = 0 \;, \tag{78}$$

where $\tilde{s} = (2\ell + 1)s$. We note that $\text{Im}\,\Omega$ obtained from this equation becomes ∞ as $\tilde{s} = (2\ell + 1)s \to \infty$, unlike the case of Eq. (20). This suggests that the fastest growing mode of this simplified system has the infinite growth rate with $\ell = \infty$. We, however, do not worry about this point here, either, assuming that such high-radial eigenmodes be damped in reality by some perpendicular diffusion that is not explicitly included in the system of Ref. 8. In addition to these assumptions, however, Connor assumed that the inertia $\partial\phi/\partial\tau$ of Eq. (5) be dropped, which is crucial to obtain the explicit form of χ_i given by Eq. (77). This assumption is equivalent to ignoring the first term of Eq. (78) and the linear growth rate is now given by

$$\Omega = \frac{is\,K}{1 - \tilde{k}^2 K} \;. \tag{79}$$

It is clear that, as $\tilde{k}^2 = k_y^2 \rho_s^2 \to 1/K$, the linear growth rate approaches ∞ while the coefficient of the second term of Eq. (78) approaches 0. It follows that dropping the first term of Eq. (78) or dropping the inertia $\partial\phi/\partial\tau$ from Eq. (5) may not be justified. In fact, eliminating the first term Ω^2 of Eq. (78) prevents the thermal mode from being excited, which is the main mechanism of the η_i-mode, as discussed in Sec. III. We thus conclude that

the assumption made in Ref. 8 leads to oversimplification of the original system, and this oversimplified system no longer possesses the qualitatively correct linear properties of the η_i-mode.

(B) The work by Lee and Diamond [Ref. 9]

In Ref. 9, Lee and Diamond derive from the system (5)–(7)

$$\chi_i = g\,\frac{\rho}{L_n}\left(\frac{cT_e}{eB}\right) K^2 s(k_y\,\rho_s)_{\mathrm{rms}} , \tag{80}$$

where $(k_y\,\rho_s)_{\mathrm{rms}} \simeq 0.4$ and g is a weak function of η_i. The essence of this work is well represented in their subsection A "Heuristic description" of Sec. III of Ref. 9. In this subsection, based on the so-called one-point renormalized equation, they derived the following two relations (Eqs. (36) and (38) in Ref. 9)

$$D_k \simeq K^{1/2}\, k'_{\|}\, \Delta_k^3$$

$$\Delta_k \simeq (D_k/k'_{\|})^{1/4}$$

by balancing certain key terms of the system. Here D_k is the k-dependent anomalous diffusion coefficient arising from the nonlinearity $\{\phi, p\}$, or the $\mathbf{E} \times \mathbf{B}$ convection of the pressure fluctuation, Δ_k is the k-dependent radial correlation length and $k'_{\|} = k_y/L_s$. These relations lead to the decorrelation rate $\Delta\omega_k(= D_k/\Delta_k^2)$ associated with $\mathbf{E} \times \mathbf{B}$ turbulent convection and the radial correlation length Δ_k given by

$$\Delta\omega_k \propto s\,K \tag{81}$$

$$\Delta_k \simeq \sqrt{K} , \tag{82}$$

which basically corresponds to the choice made to derive Eq. (47) in Sec. III. This balancing of certain linear terms of the system is essentially equivalent to the approximation that Connor made in Ref. 8, leading to the linear growth rate of Eq. (79) with the extra assumption $\tilde{k}^2 K \ll 1$, i.e.,

$$\Omega \simeq is\,K . \tag{83}$$

41

Thus, it is not just a coincidence that the shear dependence of χ_i given in Refs. 8 and 9 are the same. Since the one-point renormalized equations, in which all the nonlinear convection terms are simply replaced by linear diffusion terms with diffusion coefficients to be determined, give a linear system, one must use the linear properties of the system one way or another at some point if he wishes to evaluate fluctuation levels and anomalous transport coefficients from the one-point renormalized equations. In this sense, it is not clarified nor justified in Ref. 9 why these authors choose the particular way of balancing the terms that lead to the linear growth rate of Eq. (83) (which was subsequently used as the decorrelation rate $\Delta\omega_k$ of Eq. (81) and rule out the possibility of balancing different terms in such a way that a larger growth rate $\mathrm{Im}\,\Omega \propto \sqrt{s\,K}$ with $k^2\,\rho_s^2 \simeq 1/K$ is obtained. Although it is observed in numerical simulations that the modes with smaller $k_y\,\rho_s$ have larger amplitude in the turbulent state, these modes are produced by nonlinear interactions of higher-k_y primary modes and not by the strong linear instability. In fact, these nonlinearly excited low-k_y modes have different mode properties from the linearly excited low-k_y modes. Therefore, detailed justification is needed if one attempts to associate the properties given in Eqs. (81) and (82) of the long wavelength linear eigenmodes $k^2\,K \ll 1$ with the nonlinearly excited low-k_y modes. We also note that Lee and Diamond relate the pressure fluctuation $\tilde{p}_k$ to the electrostatic potential fluctuation $\tilde{\phi}_k$ as

$$\tilde{p}_k \simeq i\,K\,\omega_{*e}\,\tilde{\phi}_k/\Delta\omega_k \ , \tag{84}$$

(Eq. (35) of Ref. 9) by balancing the anomalous diffusion term to the ion-temperature gradient driven term in their one-point renormalized equations. Using the relation Eq. (84) is in fact crucial to obtain an explicit form of the anomalous diffusion coefficients from their two-point renormalization technique presented in their subsection B of Sec. III of Ref. 9. Despite their elaboration of the two-point renormalization technique, therefore, the final results derived therein (such as Eq. (85) and Eq. (97) of Ref. 9) heavily depend on the choice

42

of the unjustified linear-like relation Eq. (84) taken from the *one-point* equations. This approximation makes obscure the accuracy of the conclusions of the two-point renormalization technique in Ref. 9.

(C) The work by Terry [Ref. 10]

Terry *et al.* derive the anomalous diffusion coefficient given by

$$D_k \simeq \omega_* \rho_s^2 (2\ell + 1)^2 K^2 s \tag{85}$$

(Eq. (10) of Ref. 10) to the lowest order of s, from the system (5)–(7), using the mixing length estimate and the one-point renormalization technique. It is claimed that the larger radial eigenmode number ℓ ($1 \leq \ell \lesssim 10$) significantly increases D_k over the D_k obtained by Lee and Diamond in Ref. 9 as the higher-order radial eigenmodes are more strongly excited and bear a broader mode structure. Since the method used to obtain the scaling of Eq. (85) is similar to that of Ref. 9, the critique to Ref. 9 presented above also applies to Ref. 10. In addition, it seems inconsistent that the authors of Ref. 10 maximize the growth rate by varying the radial mode number ℓ while keeping k_y (or the poloidal mode number m) small i.e., $k_y^2 \rho_s^2 K \ll 1$. Also, as noted before, the radial eigenmode number ℓ that gives the largest growth rate is also a strong function of s. Therefore, the scaling of Eq. (85) does not show the shear dependence of D_k explicitly.

These critiques and the fact that none of these previous works[8–10] provide nonlinear simulations supporting their results indicate that these previously reported χ_i-scalings are not justified. Given the more rigorous analyses and direct numerical simulations of the system (5)–(7) presented in the present work, therefore, we conclude that, in the parameter range $sK \lesssim 1$ of interest for tokamak plasmas, the χ_i-scalings reported in Refs. 8-10 are erroneous and that the correct scaling of χ_i due to the η_i-mode turbulence in a sheared slab geometry is given by Eq. (75). Other properties of the η_i-mode in tokamaks due to toroidicity and kinetic effects are, of course, beyond the scope of the present work.

43

Acknowledgments

References

1. M. Greenwald, D. Q. Winn, S. Milora, R. Parker, and S. Wolfe, Phys. Rev. Lett. **53**, 352 (1984).

2. F.X. Sölder, E.R. Müller, F. Wagner, *et al.* Phys. Rev. Lett. **61**, 1105 (1988).

3. R.J. Fonk, R. Howell, K. Jaehnig, L. Roquemore, G. Schilling, S. Scott, M.C. Zarnstorff, C. Bush, R. Goldston, H. Hsuan, D. Johnson, A. Ramsey, J. Schivell, and H. Towner, Phys. Rev. Lett. **63**, 520 (1989).

4. D.L. Brower, W.A. Peebles, S.K. Kim, N.C. Luhmann, W.M. Tang, and P.E. Phillips, Phys. Rev. Lett. **59**, 48 (1987).

5. L.I. Rudakov and R.Z. Sagdeev, Dokl. Akad. Nauk. SSSR **138**, 581 (1961) [Sov. Phys. Dokl. **6**, 415 (1961).

6. B. Coppi, M.N. Rosenbluth, and R.Z. Sagdeev, Phys. Fluids **10**, 582 (1967).

7. W. Horton, R.D. Estes and D. Biskamp, Plasma Physics **22**, 663 (1980).

8. J.W. Connor, Nucl. Fusion **26**, 193 (1986).

9. G.S. Lee and P.H. Diamond, Phys. Fluids **29**, 3291 (1986).

10. P.W. Terry, J.-N. Leboeuf, P.H. Diamond, D.R. Thayer, J.E. Sedlak, and G.S. Lee, Phys. Fluids **31**, 2920 (1988).

11. To be precise, there are slight differences (such as the diffusion terms taken into account) between the systems used in Refs. 7, 8, 9, and 10. However, it is easy to show that these differences do not account for the different scalings of χ_i stated in the text.

12. W. Horton, D.-I. Choi, and W. M. Tang, Phys. Fluids **24**, 1077 (1981).

13. F. Romanelli, W.M. Tang, and R.B. White, Nucl. Fusion **26**, 1515 (1986).

14. F. Romanelli, Phys. Fluids **B1**, 1018 (1989).

15. P.N. Guzdar, L. Chen, W.M. Tang, and P.H. Rutherford, Phys. Fluids **26**, 673 (1983).

16. R.R. Dominguez and R.E. Waltz, Nucl. Fusion **27**, 65 (1987).

17. B.-G. Hong and W. Horton, Plasma Physics and Controlled Fusion **31**, 1291 (1989).

18. S.I. Braginskii, in *Review of Plasma Physics*, ed. by M.A. Leontovich (Consultant Bureau, New York, 1965), Vol. 1, p. 205.

19. W.M. Tang, G. Rewoldt, and L. Chen, Phys. Fluids **29**, 3715 (1986).

20. T.S. Hahm and W.M. Tang, Phys. Fluids **B1**, 1185 (1989).

21. S. Hamaguchi, Phys. Fluids **B1** 1416 (1989).

22. D.D. Joseph, Stability of Fluid Motion, Vols. I and II (Springer, New York, 1976).

23. W. Park, D.A. Monticello, R.B. White, and A.M.M. Todd, Bull. Amer. Phys. Soc. **23**, 779 (1978).

24. H.R. Strauss, W. Park, D.A. Monticello, R.B. White, S.C. Jardin, M.S. Chance, A.M.M. Todd, and A.H. Glasser, Nucl. Fusion **20**, 628 (1980).

25. R.E. Waltz, W. Pfeiffer, and R.R. Dominguez, Nucl. Fusion **20**, 43 (1980).

26. J.Q. Dong, P.N. Guzdar, and Y.C. Lee, Phys. Fluids **30**, 2694 (1987).

Figure Captions

1. The contours of constant linear growth rate γ as functions of k_y and $k_\parallel$ obtained from Eqs. (5)–(7) under the local assumption. Here k_x is chosen so as to maximize $\gamma = \gamma(k_x, k_y, k_\parallel)$. The solid lines represent $\gamma \geq 0$ and the dotted lines represent $\gamma < 0$. In (a), $K = 3.0, \Gamma = 2.0, \mu_\parallel = \chi_\parallel = 1.0$ and $\mu_\perp = \chi_\perp = 0$. The maximum of $\gamma = 0.28\, c_s/L_n$ is obtained at $k_y \rho_s = 0.82$ and $k_\parallel L_n = 0.41$. The difference between the two contour lines indicates $\Delta\gamma = 1.2 \times 10^{-2}\, c_s/L_n$. In (b), all the parameters are the same as those in (a) except $\mu_\perp = \chi_\perp = 0.1$. The maximum of $\gamma = 0.22\, c_s/L_n$ is obtained at $k_\parallel L_n = 0.34$ and $k_y \rho_s = 0.73$. The difference between the two contour lines indicates $\Delta\gamma = 0.90 \times 10^{-2}\, c_s/L_n$.

2. The growth rate γ (normalized by c_s/L_n) as a function of $\tilde{s} = (2\ell + 1)s$ and $k = k_y \rho_s$ calculated from Eq. (20). The parameters are $K = 3.0$, $k = 0.2m$ $(1 \leq m \leq 10)$, and $\Gamma = \mu_\parallel = \chi_\parallel = \mu_\perp = \chi_\perp = 0$. The growth rate γ attains its maximum value $0.753\, c_s/L_n$ at $\tilde{s} = 7.65$ and $K = 1.4$.

3. The largest growth rate $\gamma_{\max}$ (normalized by c_s/L_n) as a function of the shear s, calculated from Eq. (20). All the parameters used here are the same as those in Fig. 2. The mode numbers ℓ and m are chosen so as to maximize γ. For $s \geq 4.1$, the $\ell = 0$ mode is dominant and for $1.8 \leq s \leq 4.1$, the $\ell = 1$ mode is dominant.

4. The growth rates expressed by $\mathrm{Im}\,\Omega$ for the fundamental ($\ell = 0$) mode with $\mu_\perp = \chi_\perp = 0$. The solid lines are obtained from the shooting code solving Eq. (19) and the broken lines from the theory [Eq. (39)]. The two cases, $\Gamma = 0$ and $\Gamma = 2$, are presented. (a) $\mu_\parallel = \chi_\parallel = 1.0$, $s = 0.1$ and $k = k_y \rho_s = 0.5$. (b) $\mu_\parallel = \chi_\parallel = 2.0$, $K = 2.0$ and $k = 0.2$.

5. The largest growth rate $\gamma_{\max}$ (normalized by c_s/L_n) as a function of s, calculated by the linear initial value code. The parameters used here are $K = 3.0$, $\Gamma = 2$, $\mu_\parallel = \chi_\parallel = 1.0$ and $\mu_\perp = \chi_\perp = 0.01$. The wavenumber $k = 0.2\,m$ are chosen so as to maximize γ. For $s \geq 0.15$, the $m = 3$ mode is most strongly excited while for $s < 0.15$ the $m = 4$ mode is most strongly excited.

6. The anomalous diffusion coefficients D as a function of s, calculated from the mixing length theory or $\tilde{\gamma}\,\Delta_x^2$. The linear growth rate $\tilde{\gamma}$ and the mode width Δ_x are evaluated from the most unstable linear mode obtained from the linear initial value code. The mode width Δ_x is defined by $\Delta_x^{-2} = \langle (d\phi/dx)^2 \rangle / \langle \phi^2 \rangle$. Near $s = 0.1$, D scales as $s^{-1/2}$.

7. Time evolution of the total energy E_T obtained from the single-helicity calculation, where $K = 3.0, s = 0.1, \Gamma = 2, \mu_\parallel = \chi_\parallel = 1.0$ and $\mu_\perp = \chi_\perp = 0.01$. The domain is $|x/\rho_s| \leq L_x = 40$ and $L_y = 10\pi$. Seven modes ($0 \leq m \leq 6$) are included in this calculation with $k_y\,\rho_s = 0.2$ for the $m = 1$ mode.

8. The contours of constant ϕ at $\tau = t\,c_s/L_n = 500$, obtained from the long-time extension of the simulation shown in Fig. 7.

9. The contours of constant ϕ at saturation with larger shear $s = 0.5$ obtained from the single-helicity calculation. The other parameters are the same as those used in Figs. 7 and 8, except for $L_x = 20$. The nonlinearly saturated modes are more strongly localized to the mode rational surface at $x/\rho_s = 0$.

10. Fourier cosine components of the perturbed pressure $\tilde{p}_i$ at $\tau = 500$ of the same calculation as Fig. 8. The dominant $m = 0$ (or $k_y = 0$) mode that locally cancels the background constant ion pressure gradient K.

11. The anomalous ion heat conductivity χ_i as a function of s, obtained from the single-helicity simulations. The parameters used in the simulations are $K = 3.0$, $\Gamma = 2$,

$\mu_\parallel = \chi_\parallel = 1.0$ and $\mu_\perp = \chi_\perp = 0.01$. The domain is $L_x = 40$ for $\triangle$, $L_x = 20$ for $\bullet$, and $L_y = 10\pi$ for both. The solid curve indicates the scaling of $\chi_i = \chi_0 \exp(-\alpha s)$ with $\chi_0 = 5.34 \times 10^{-2}$ and $\alpha = 7.2$. The error bars represent the fluctuation level defined by Eq. (72).

12. The anomalous ion heat conductivity χ_i as a function of $K - K_c$, obtained from the single-helicity simulations. The parameters used in the simulations are $s = 0.1$, $\Gamma = 2$, $\mu_\parallel = \chi_\parallel = 1.0$, $\mu_\perp = \chi_\perp = 0.1$, and $K_c = 0.4$. The domain is given by $L_x = 20$ and $L_y = 10\pi$. The solid line is the curve proportional to $(K - K_c)$.

13. Time evolution of the total energy $E_\perp$ obtained from the 3D calculation with 130 modes ($0 \le m \le 9$ and $-6 \le n \le 6$). The parameters used here are $K = 3.0$, $s = 0.1$, $\Gamma = 2$, $\mu_\parallel = \chi_\parallel = 1.0$, and $\mu_\perp = \chi_\perp = 0.1$. The turbulent saturation is observed at $\tau = t\, c_s/L_n \simeq 50$.

14. Time evolutions of the perpendicular kinetic energy $E_{\perp mn}$ of four sampled (m, n)-modes are plotted under the same conditions as in Fig. 13. In this case, the $m = 4$ modes are linearly most unstable. However, after saturation, the modes with $m \le 3$ reach the energy levels similar to those of the $m = 4$ modes.

15. The perpendicular kinetic energy spectrum $E_{\perp m}$ obtained from the time average of $\sum_n E_{\perp mn}$ over $60 \le t\, c_s/L_n \le 100$ under the same conditions as in Fig. 13. The modes with $m \le 4$ have relatively high energy levels with the peak at $m = 3$ (or $k_y\, \rho_s = 0.6$) while the modes with $m \ge 5$ are significantly weaker.

16. The contours of constant ϕ at $\tau = t\, c_s/L_n = 100$ from the simulation shown in Fig. 13.

17. The anomalous ion heat conductivity χ_i as a function of s, obtained from the 3D simulations. The parameters used in the simulations are $K = 3.0, \Gamma = 2, \mu_\parallel = \chi_\parallel = 10$,

and $\mu_\perp = X_\perp = 0.1$. The domain is $L_x = 20$, $L_y = 10\pi$, and $L_z = 7.5\pi$. The solid curve indicates the scaling of $X_i = X_0 \exp(-\alpha s)$ with $X_0 = 1.58$ and $\alpha = 3.7$.

18. The anomalous ion heat conductivity X_i as a function of $K - K_c$, obtained from the 3D simulations. The parameters used in the simulations are $s = 0.1$, $\Gamma = 2$, $\mu_\| = X_\| = 1.0$, $\mu_\perp = X_\perp = 0.1$, and $K_c = 1.3$. The domain is the same as in Fig. 17. The solid line is the curve proportional to $(K - K_c)$.
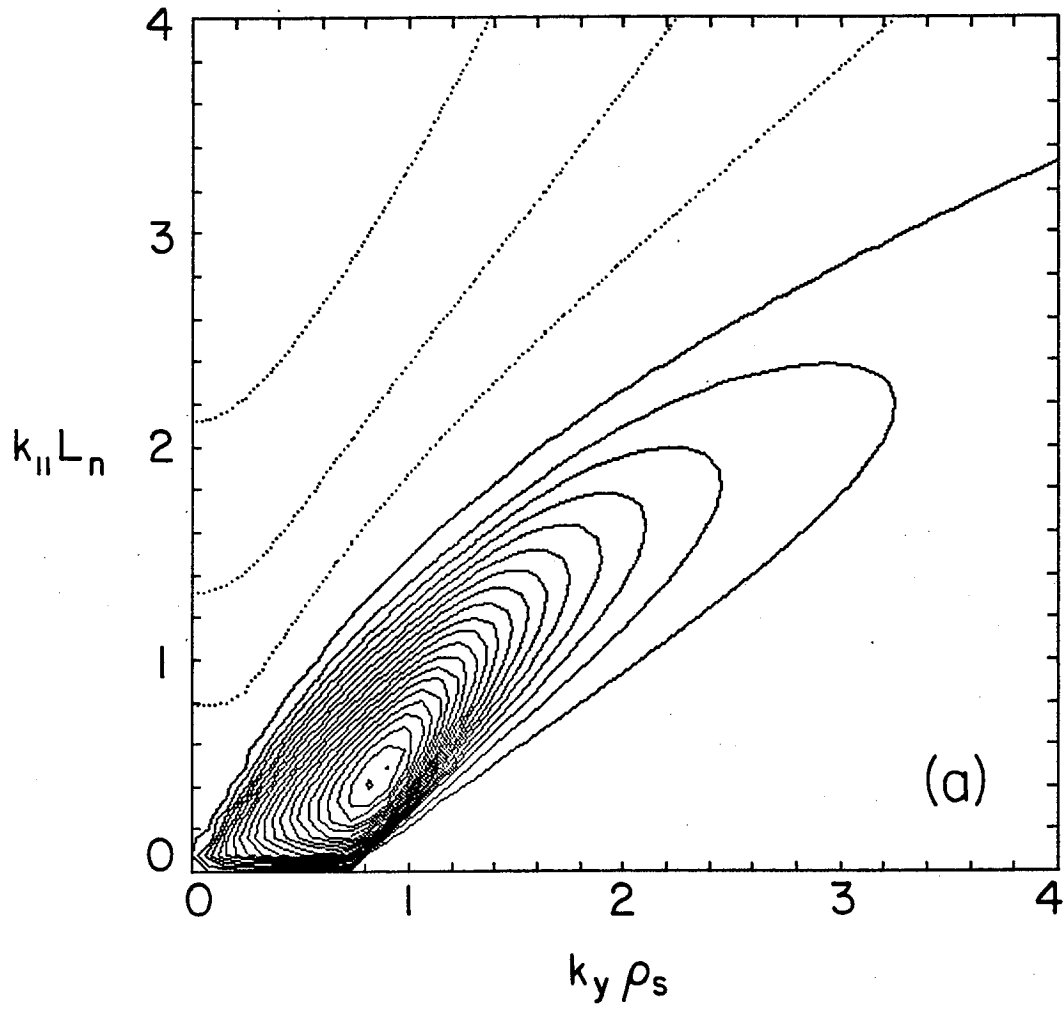
Fig. 1(a)
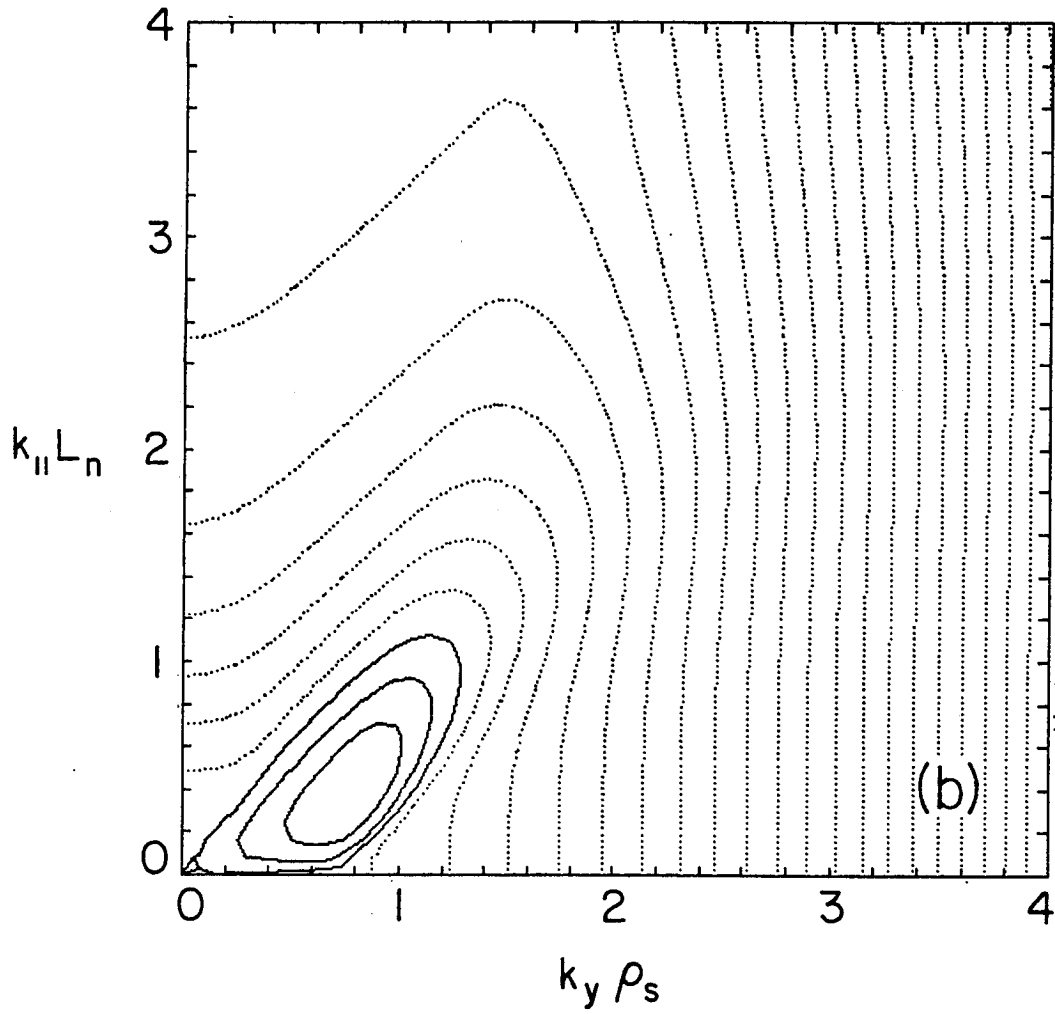
Fig. 1(b)
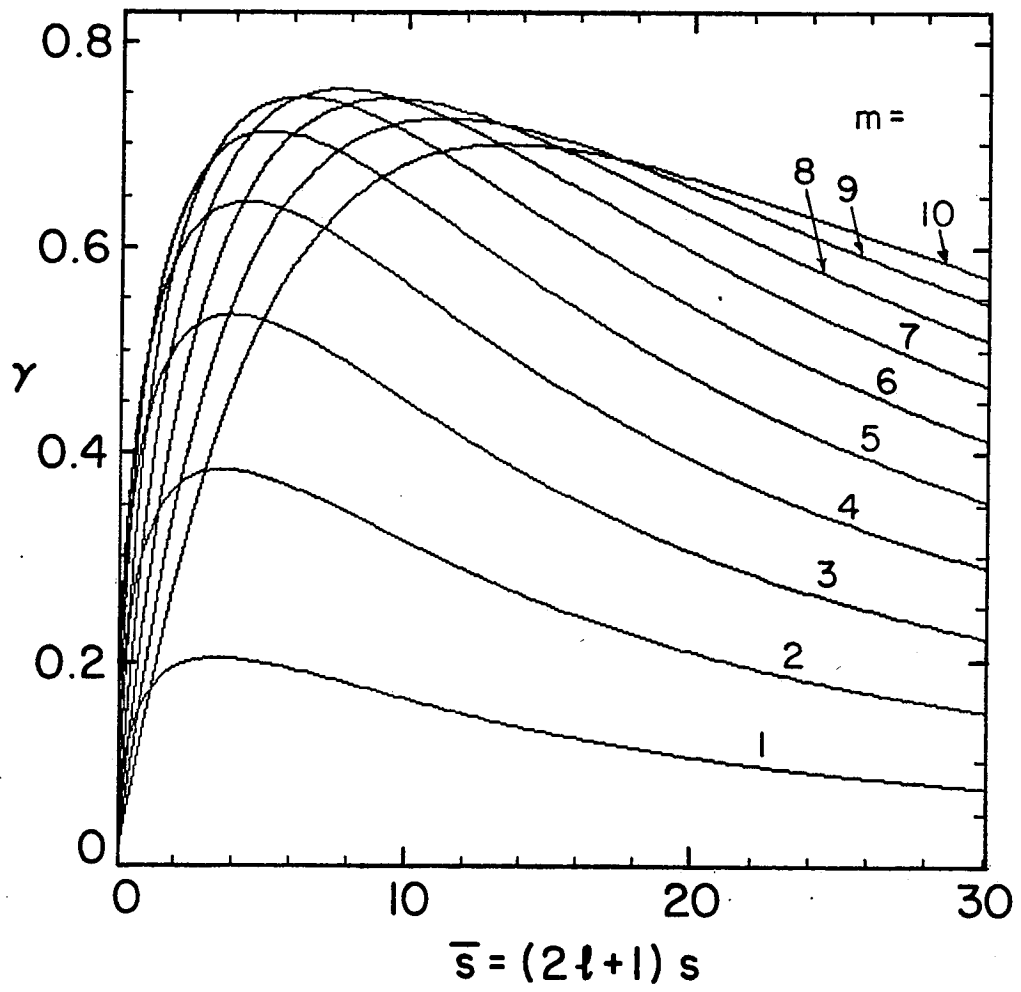
Fig. 2
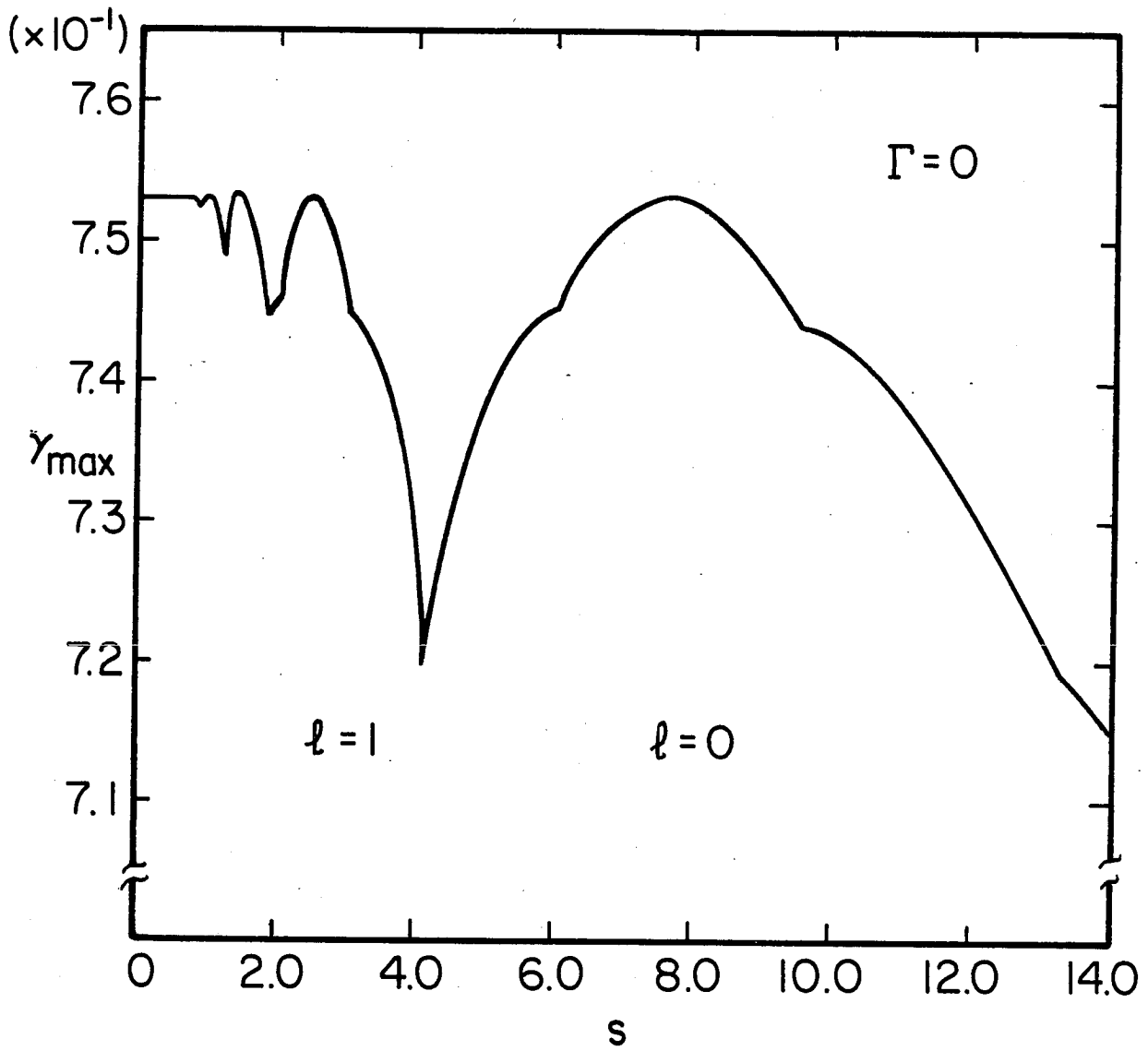
Fig. 3
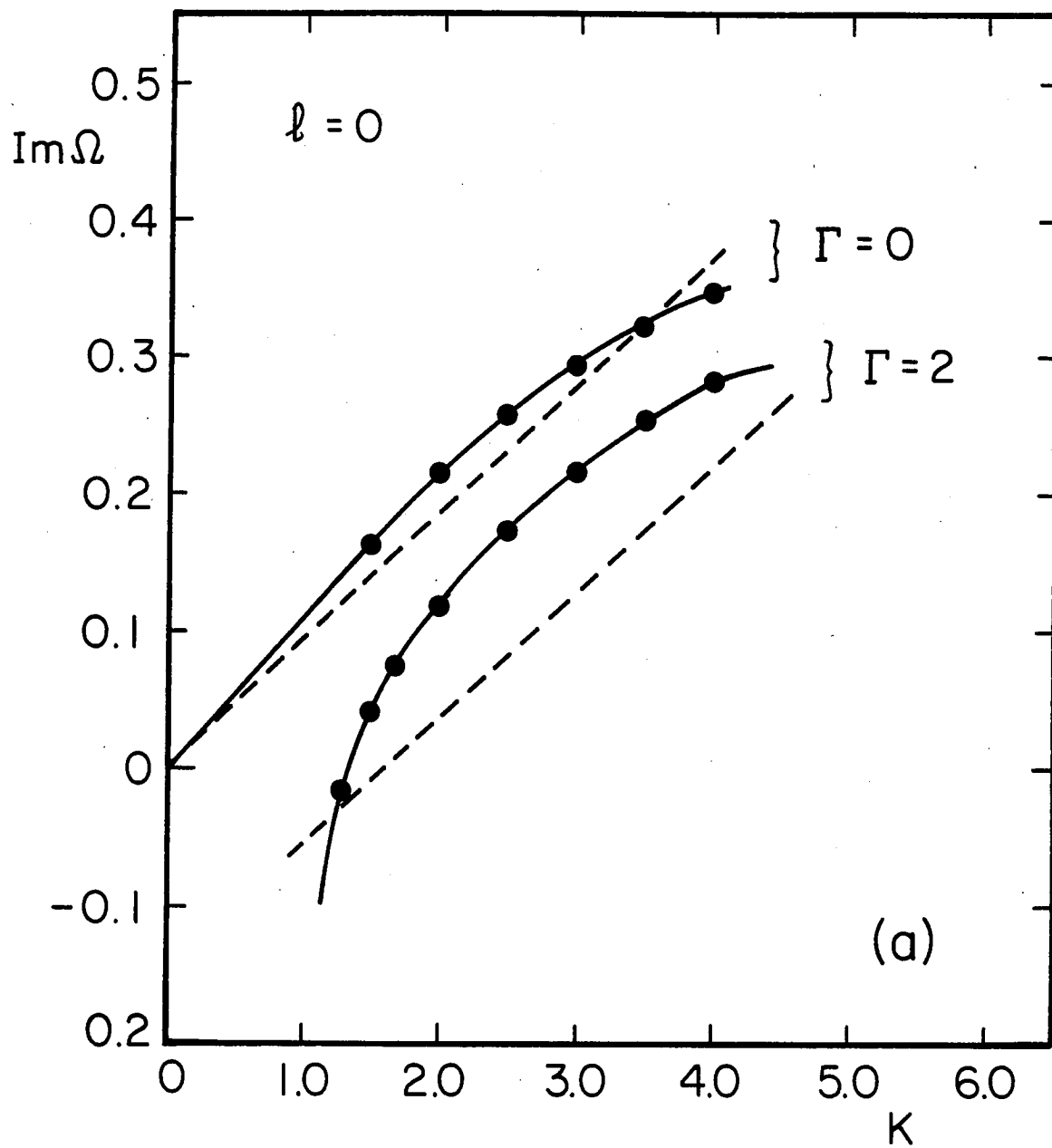
Fig. 4(a)
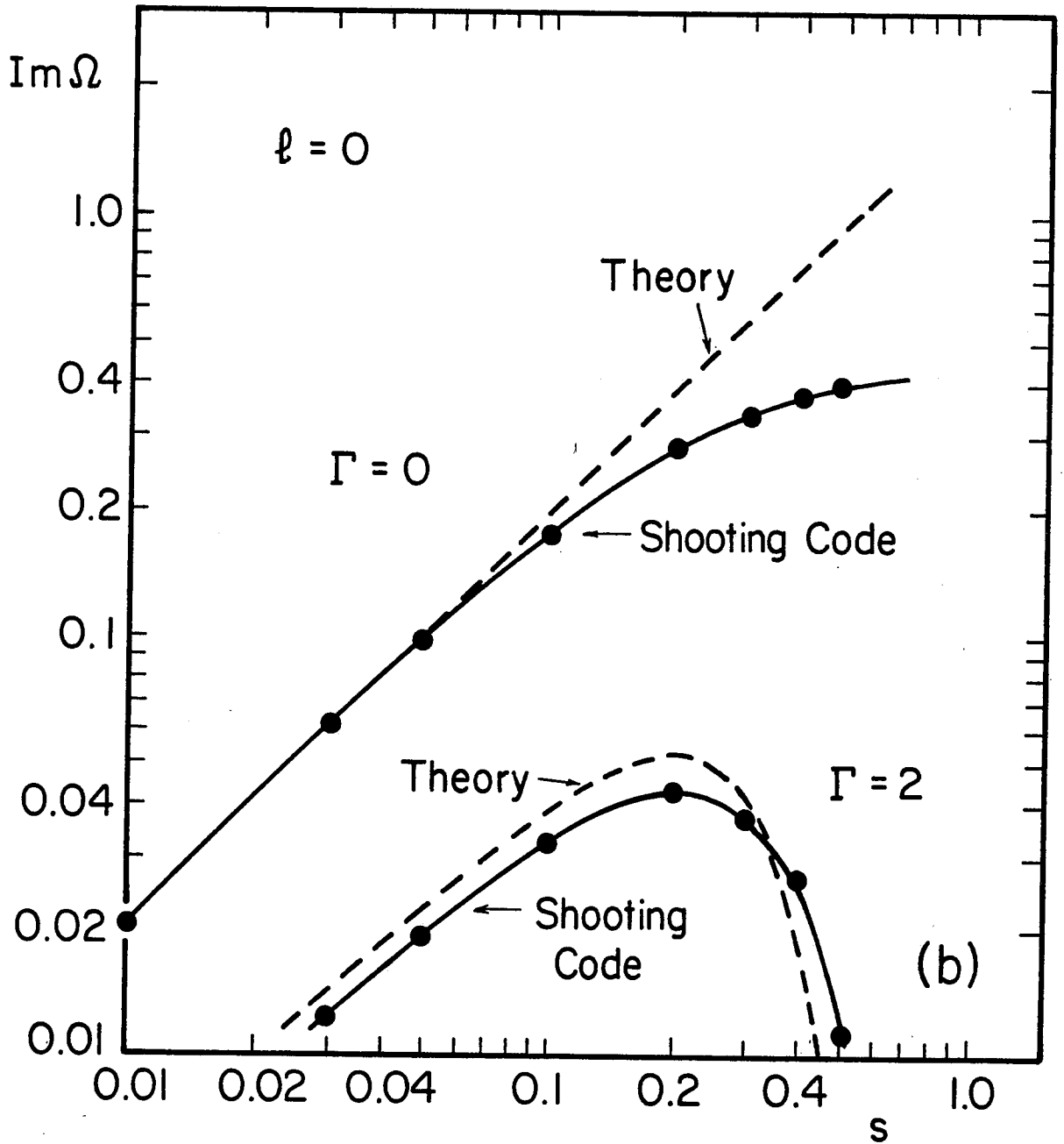
Fig. 4(b)
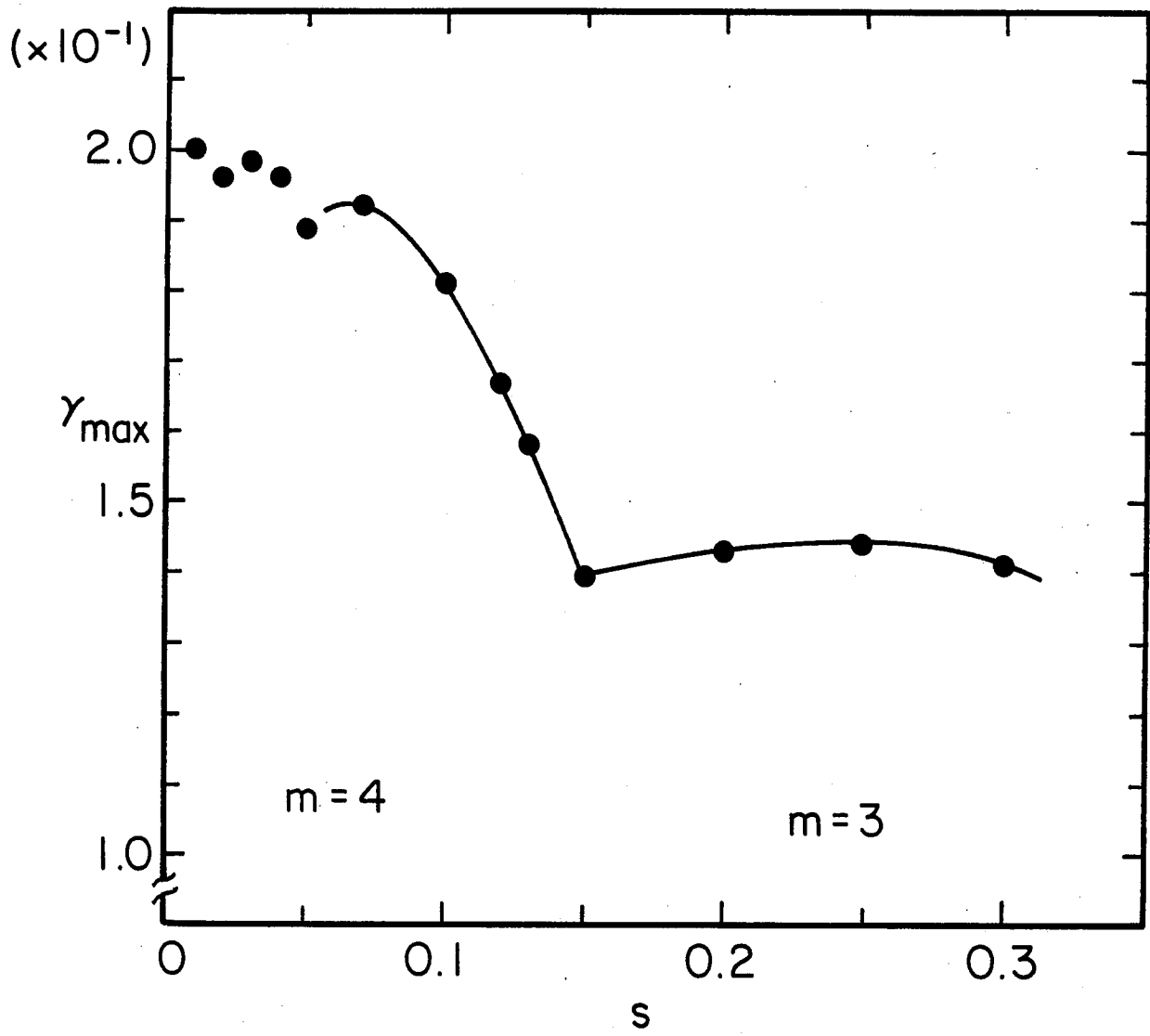
Fig. 5
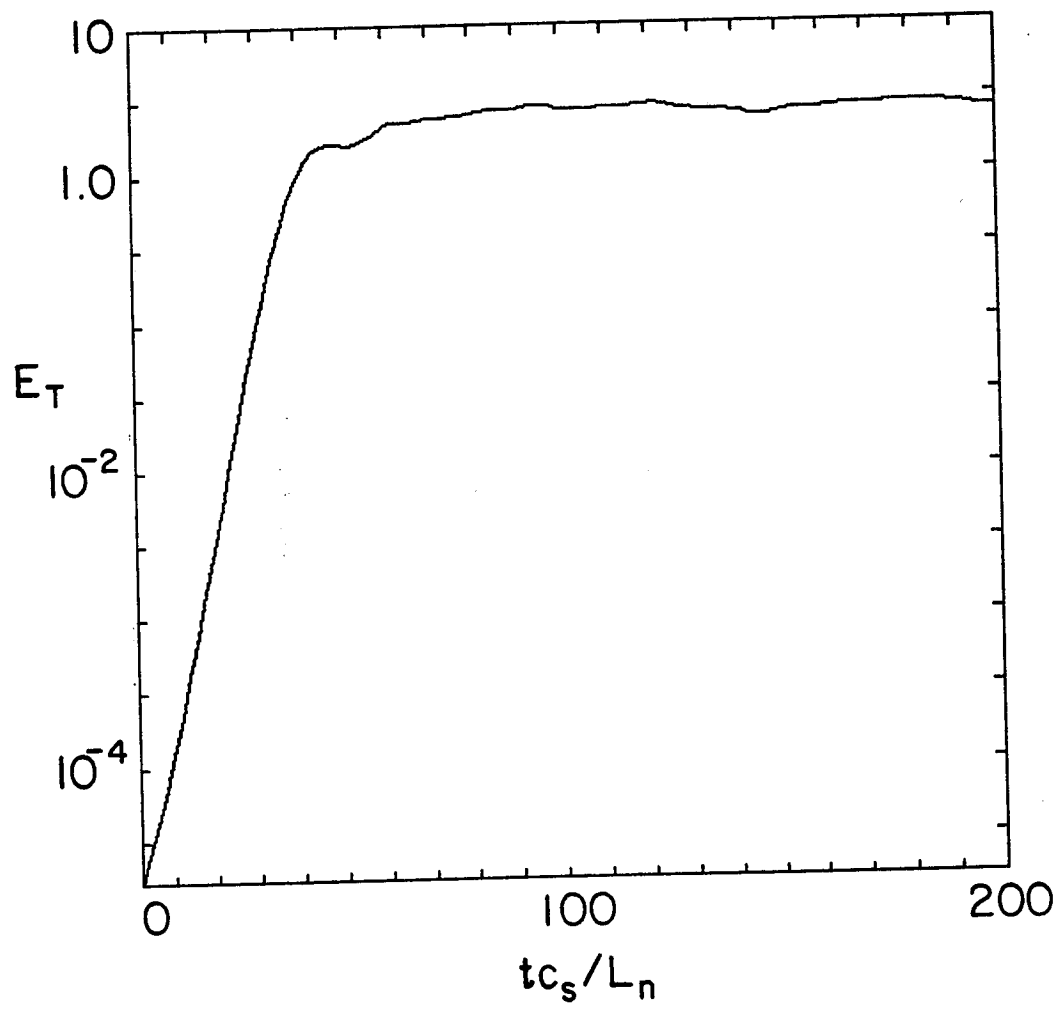
Fig. 7
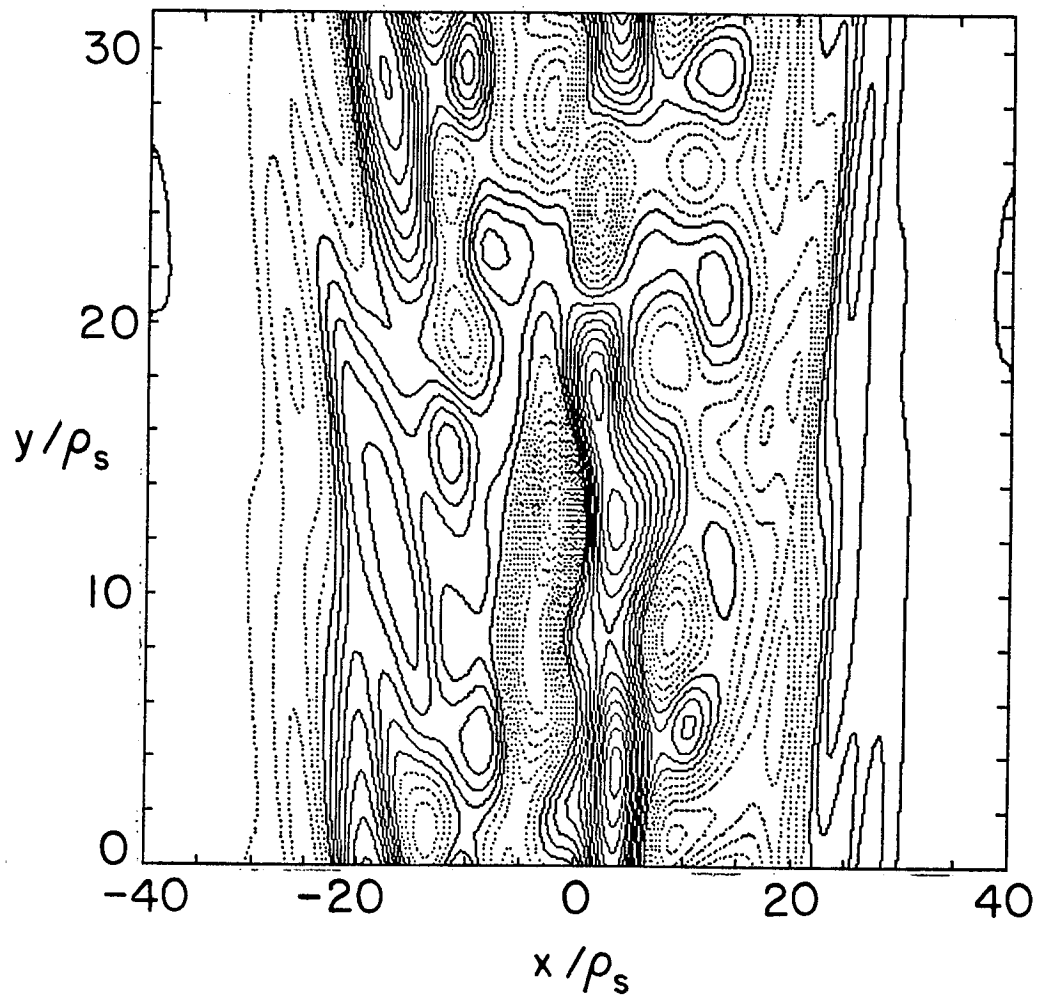
Fig. 8
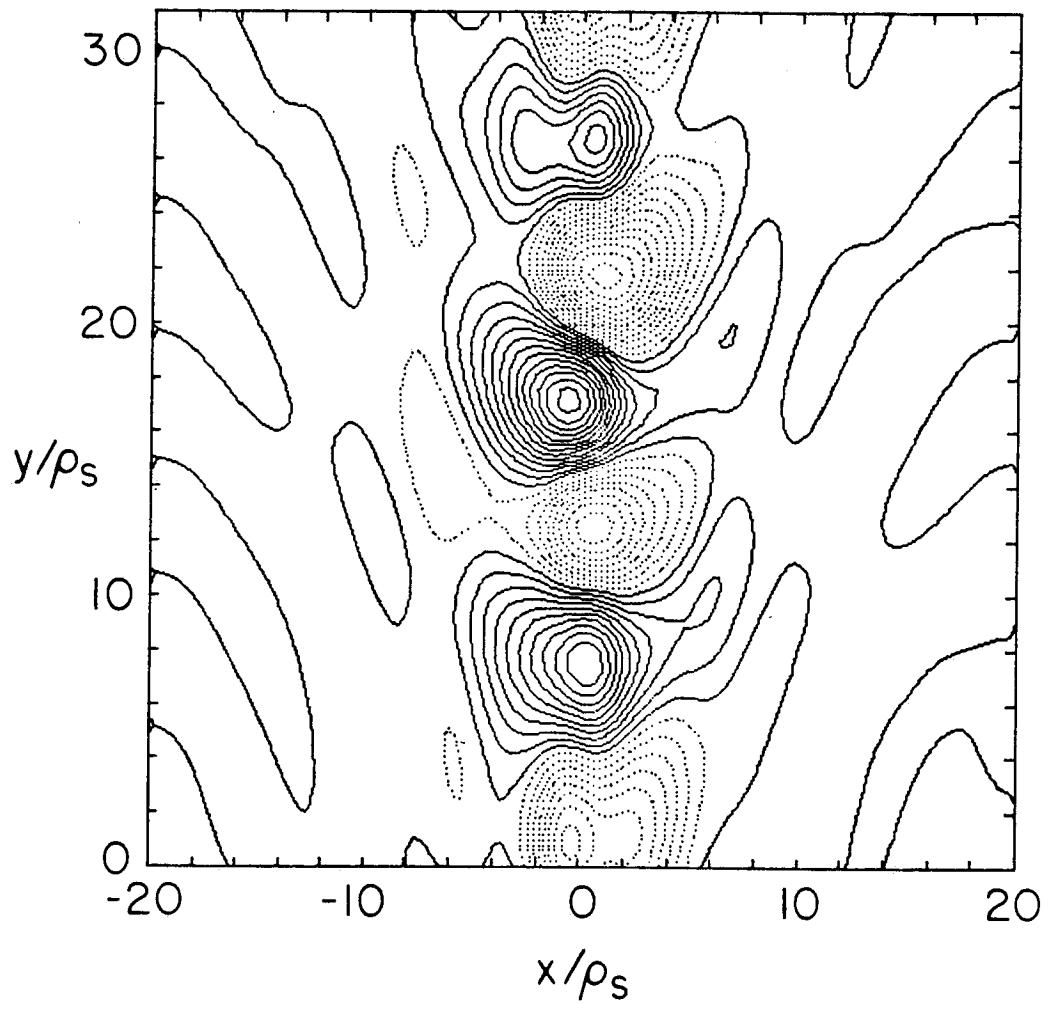
Fig. 9
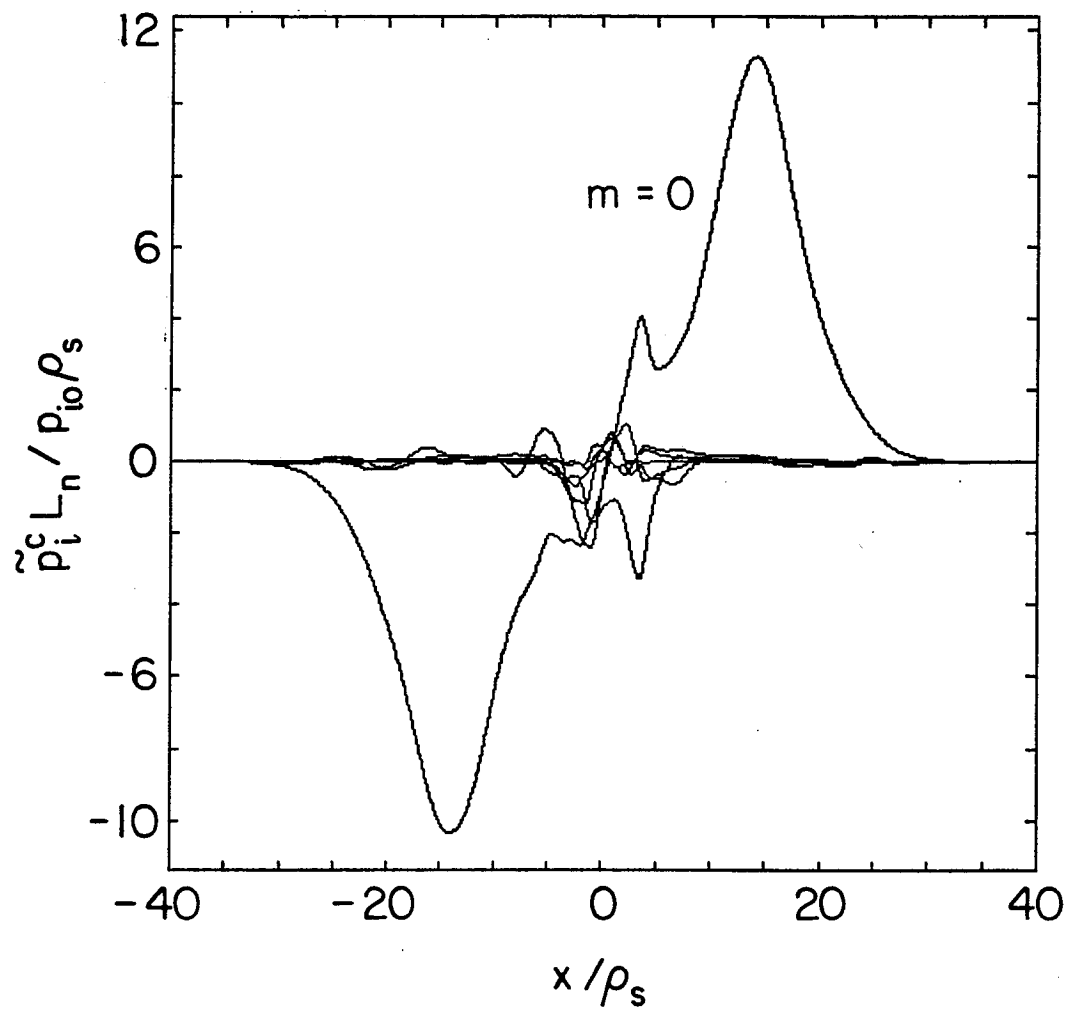
Fig. 10
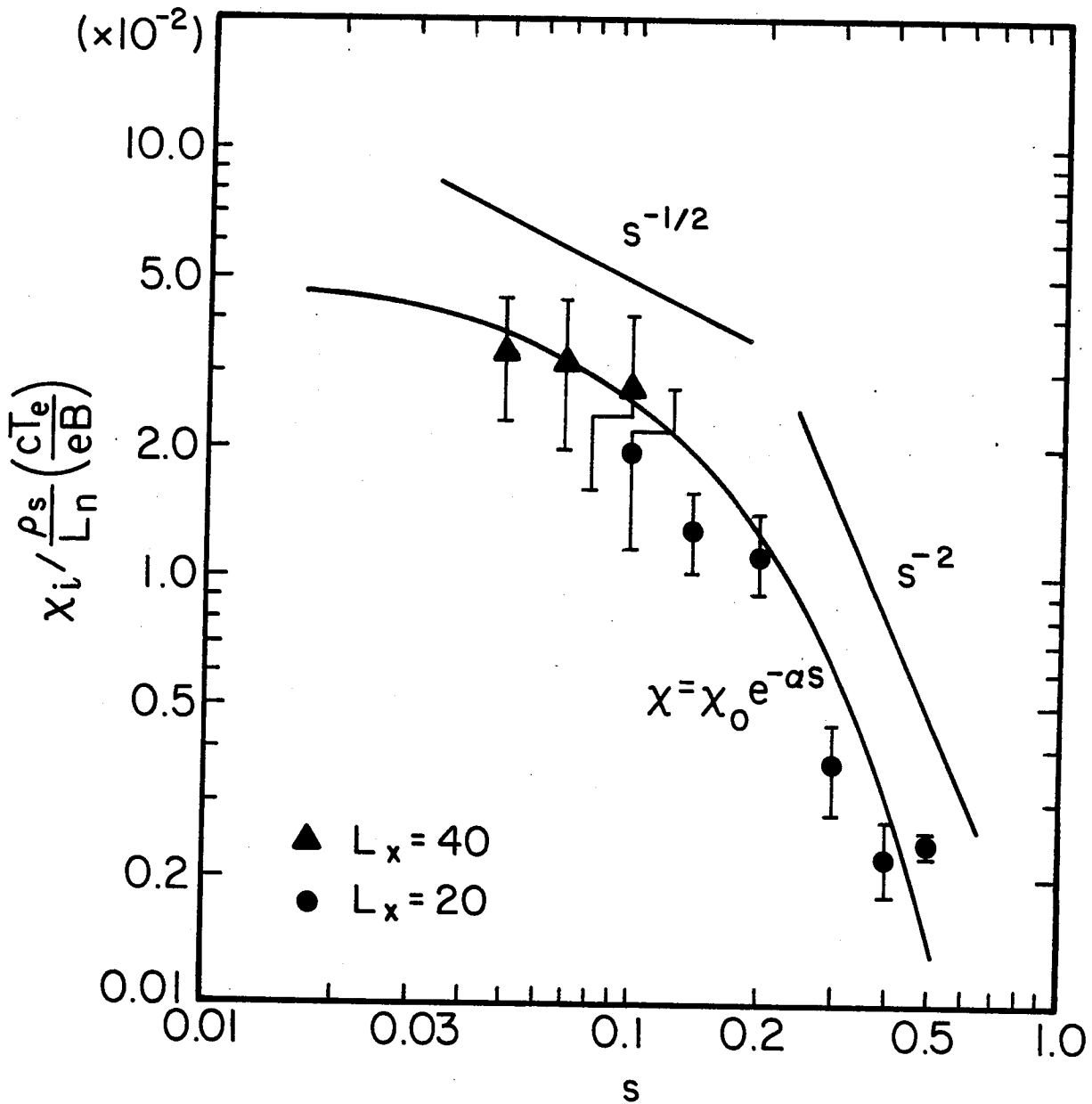
Fig. 11
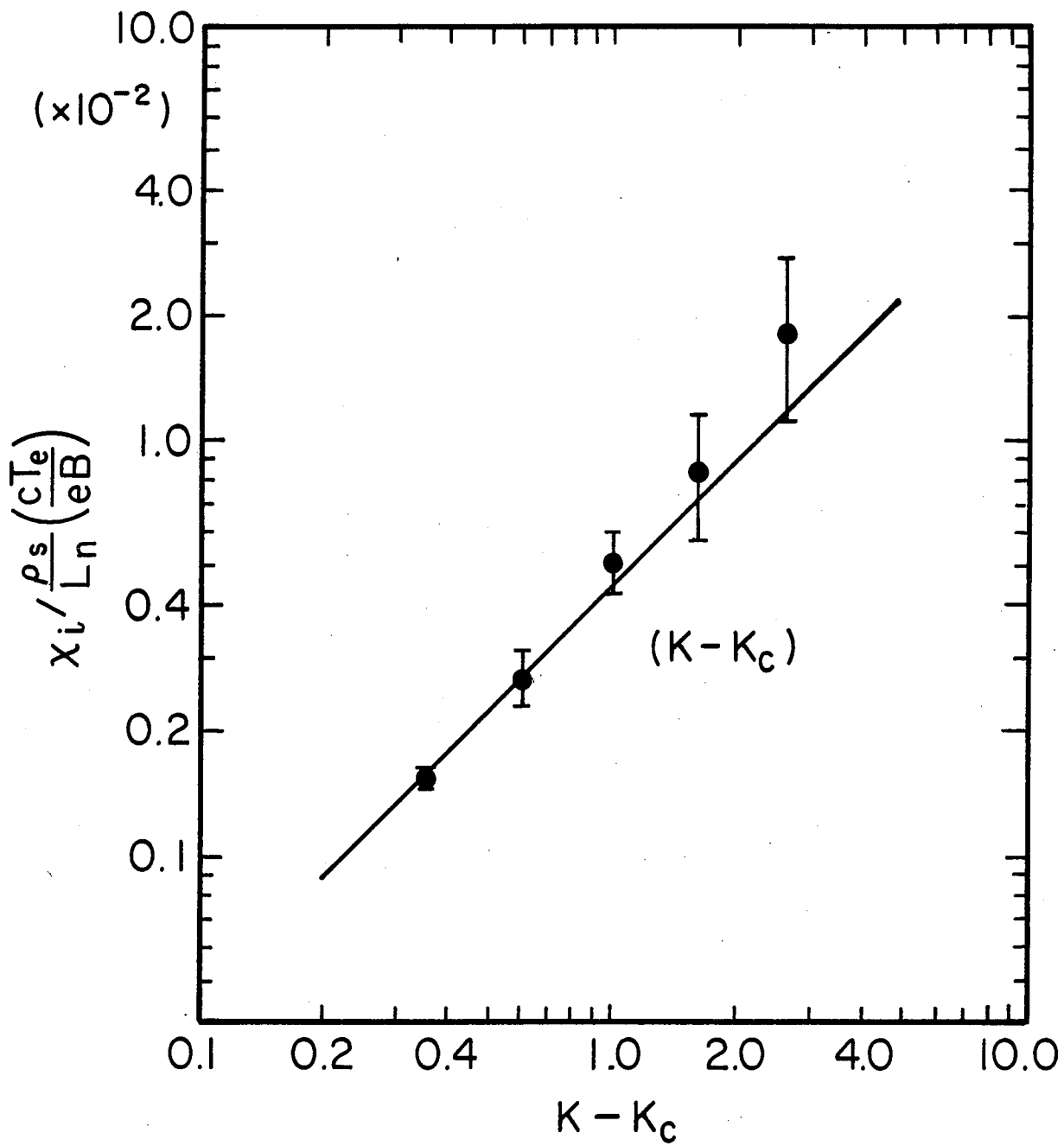
Fig. 12

Fig. 13

Fig. 14

Fig. 15

Fig. 16

The y-axis is labeled $\chi_i / \frac{\rho_s}{L_n}\left(\frac{cT_e}{eB}\right)$ with values 10.0, 5.0, 2.0, 1.0, 0.5, 0.2, 0.1. The x-axis is labeled s with values 0, 0.05, 0.1, 0.2, 0.5, 1.0. Curves are labeled $s^{-1/2}$ and $\chi = \chi_0 e^{-\alpha s}$.

Fig. 17

Fig. 18